MICROSTRUCTURE CONTROL OF AISI 4135 FOR OPTIMIZATION OF FATIGUE AND FRACTURE PERFORMANCE

A THESIS SUBMITTED TO
THE GRADUATE SCHOOL OF NATURAL AND APPLIED SCIENCES
OF

MIDDLE EAST TECHNICAL UNIVERSITY

BY

BURAK ÖZCAN

IN PARTIAL FULFILLMENT OF THE REQUIREMENTS
FOR
THE DEGREE OF MASTER OF SCIENCE

IN
METALLURGICAL AND MATERIALS ENGINEERING

JUNE 2018

Approval of the thesis:

MICROSTRUCTURE CONTROL OF AISI 4135 FOR OPTIMIZATION OF FATIGUE AND FRACTURE PERFORMANCE

submitted by **BURAK ÖZCAN** in partial fulfillment of the requirements for the degree of **Master of Science in Metallurgical and Materials Engineering Department, Middle East Technical University** by,

Prof. Dr. Halil Kalıpçılar _____
Dean, Graduate School of Natural and Applied Sciences

Prof. Dr. Cemil Hakan Gür _____
Head of Department, Metallurgical and Materials Engineering

Prof. Dr. Cemil Hakan Gür _____
Supervisor, Metallurgical and Materials Engineering Dept., METU

Examining Committee Members:

Prof. Dr. Rıza Gürbüz _____
Metallurgical and Materials Engineering Dept., METU

Prof. Dr. Cemil Hakan Gür _____
Metallurgical and Materials Engineering Dept., METU

Prof. Dr. Cevdet Kaynak _____
Metallurgical and Materials Engineering Dept., METU

Prof. Dr. A. Tamer Özdemir _____
Metallurgical and Materials Engineering Dept., Gazi University

Assist. Prof. Dr. Mert Efe _____
Metallurgical and Materials Engineering Dept., METU

Date: *07.06.2018*

I hereby declare that all information in this document has been obtained and presented in accordance with academic rules and ethical conduct. I also declare that, as required by these rules and conduct, I have fully cited and referenced all material and results that are not original to this work.

Name, Last name: Burak Özcan

Signature :

ABSTRACT

MICROSTRUCTURE CONTROL OF AISI 4135 FOR OPTIMIZATION OF FATIGUE AND FRACTURE PERFORMANCE

Özcan, Burak

M. Sc., Department of Metallurgical and Materials Engineering
Supervisor: Prof. Dr. Cemil Hakan GÜR
Co-Supervisor: Dr. Koray Yurtışık

June 2018, 85 pages

Avoiding early fatigue failure of the AISI 4135 steel shafts in trains is an important task. This study aims to improve the damage tolerance of AISI 4135 steel by modifying its microstructure via heat treatment. The overall effect of various heat treatment procedures on the damage tolerance was analyzed by considering the threshold stress intensity factor and fatigue strength. Detailed investigations on the mechanical properties were performed, and fracture surfaces were investigated. The resistance of the steel specimens having ferritic-pearlitic, bainitic and tempered-martensitic microstructure against initiation and propagation of the small flaws were demonstrated by constructing Kitagawa-Takahashi diagrams. The results showed that ferritic-pearlitic AISI 4135 axles that are being utilized in service is inappropriate, and the damage tolerance of these axles regarding the fatigue crack propagation threshold can be remarkably improved via isothermal or quench-temper applications.

Keywords: Damage tolerance, stress intensity factor, microstructure, Kitagawa-Takahas

ÖZ

YORULMA VE KIRILMA TOKLUĞU OPTİMİZASYONU İÇİN AISI 4135 ÇELİĞİNİN MİKROYAPI MODİFİKASYONU

Özcan, Burak

Yüksek Lisans, Metalurji ve Malzeme Mühendisliği Bölümü
Tez Yöneticisi: Prof. Dr. Cemil Hakan GÜR
Ortak Tez Yöneticisi: Dr. Koray Yurtışık

Haziran 2018, 85 sayfa

Bu çalışmada uygulanan ısıl işlemler ile AISI 4135 çeliğinin hasar toleransındaki iyileştirmeler sunulmuştur. Kullanım sırasında meydana gelebilecek olan yorulma hasarlarına karşı uygulanacak olan ısıl işlemlerin optimizasyonu hedeflenmiştir. Her bir ısıl işlem sürecinin aks geometrileri üzerindeki uygulanabilirliği de çalışmada ele alınmıştır. Isıl işlemlerin hasar toleransı üzerindeki genel etkisi, eşik gerilim yoğunluğu faktörü ve yorulma mukavemetleri karşılaştırılarak yorumlanmıştır. Ferritik-perlitik, beynitik ve martenzitik iç yapıların yorulma çatlaklarına karşı olan dayanımları Kitagawa-Takahashi analizi yapılarak belirlenmiştir. Mikroyapısal değişikliklerin mekanik özelliklere etkisi detaylı bir şekilde araştırılmıştır. Mikroyapısal morfolojinin hasar toleransı üzerindeki etkisi, taramalı elektron mikroskobu (SEM) ile çekilen kırık yüzey fotoğrafları baz alınarak tartışılmıştır. Uygulanan ısıl işlemler sonucunda elde edilen mikroyapıların ferritik-perlitik mikroyapısı ile karşılaştırıldığında mekanik özelliklerinin daha iyi sonuçlar verdiği gösterilmiştir. Ayrıca mikroyapısal modifikasyonlar malzemenin hasar toleransını ve gerilim yoğunluk eşik faktörünü artırarak iyileştirmiştir.

Anahtar Kelimeler: Hasar toleransı, gerilim yoğunluk faktörü, iç yapı, Kitagawa-Takahashi analizi

To my family and the beloved ones in my life,

"*The most beautiful experience we can have is the mysterious. It is the fundamental emotion that stands at the cradle of true art and true science."*

— Albert Einstein, The World as I See It

ACKNOWLEDGEMENTS

I would like to express my endless appreciation to Prof. Dr. Cemil Hakan Gür and Dr. Koray Yurtışık for their supervision, support, engagement, and encouragement throughout this study.

I am thankful to Dr. Göksu Gürer for his guidance and endless help during my master period. He helped me not only to gain knowledge and experience but also to qualify for my profession.

I am grateful to Dr. Süha Tirkeş for giving a new perspective on metallurgical engineering by their precious knowledge and curiosity on my master thesis.

I would like to thank Prof. Sir Harry Bhadeshia for his generous contribution to microstructural part of the study.

All technical expenses of this study were supported by METU Welding Technology and Non – Destructive Testing Center. I would like to thank Hafize Çakmak, Gürer Dimez, Batuhan Ersan, Eren Erol, Murat Tolga Ertürk, Burcu Anık, Mine Kalkancı, for their complimentary support.

I would like to thank technicians Kubilay Yeşildemir and Mevlüt Bağcı for their help in sample preparation part of this study.

I also would like to thank my beloved friend Büşra Özcan.

I must express my profound appreciation to my parents and brother Ayberk for providing me with unfailing support and continuous encouragement throughout years of study and through the process of researching and writing this thesis.

TABLE OF CONTENT

LIST OF FIGURES

FIGURES

LIST OF TABLES

TABLES

CHAPTER 1

INTRODUCTION

1.1. Motivation

The failure of the materials has been a crucial problem for many years due to uncontrolled environment. Most of the failures were ended up with casualties, especially in the transportation industry. As the locomotive and train industry was started to develop, failures were tremendously increased.

Fatigue failure of the steel shafts used in the delivery of mechanical power to the drivetrain is a critical issue that should be carefully tracked. According to the studies, more than 80-90% of failures and accidents in steel components and structures are assumed as directly or indirectly in relation to fatigue [1]. This assumption is supported by the studies of many structure failures conducted by researchers in Japan [2]. Atmospheric effects, foreign particle collusion, inherent material defects, mechanical contact, and the poor machining quality lead initiation of small surface cracks, which in turn, unexpected failure of the component. Since the outer effects could not be eliminated, improvement in the useful lifetime by changing the chemical composition and microstructure has become the main focus of the research activities. The casualties such as Versailles train accident (1842), Norwegian Service Flight 451 accident (1997) or “Ride the Ducks” crash (2015) are all addressed by the unexpected failure of load carrying steel axles [3, 4].

Figure 1 An illustration of Versailles train accident [5]

Although many techniques and analysis methods were developed, unforeseen fractures on axles were inevitable. However, fractures are not the results of the failures, they are the cause of the failures. Therefore, modification of either design or material itself is required to obtain durable structures.

1.2. Aim and Main Contribution

This study aims to determine the optimum microstructure in order to obtain the most reliable interval and crack size limit between two successive NDT inspection. The fitness-for-service concept was used to obtain the most damage tolerant modified microstructure for the AISI 4135 steel. Allowable stresses and defect sizes were specified with respect to the modified microstructures by evaluating mechanical and physical properties of the materials. The inferiority of current axle microstructure configuration was presented, and microstructures were investigated in terms of not only metallurgical but also mechanical approaches.

The study differs from the other studies in literature since it indicates the relationship between mechanical properties and modified fatigue limits by changing surface crack sizes. A comprehensive research on structural reliability in terms of not only the static but also the dynamic mechanical behavior of different heat treatments was carried out in this study.

CHAPTER 2

THEORY AND LITERATURE

2.1. History and Literature Review

Steel is one of the common materials used in advance manufacturing industries such as transportation, aerospace, automotive, marine, defense, etc. due to its versatility, low-cost, formability, uniformity, strength, and recyclability [6]. In the beginning, steel was commonly used for military purposes as weapons, shields, and components for vehicles. When steel was adapted to civil life, it was started to use as structural material. The latter usage was in rail transportation industry.

After the introduction of Bessemer technique for steel casting, railway transportation was on the verge of an important breakthrough with the introduction of steel rails and tracks [7]. In following years, right after the first fully working railway steam locomotive was built, steel axle was started to utilize in rotating part industry [6]. After 1830, as locomotives were used for transportation and it was accepted as a landmark in civil progress [3]. However, it was the first time that metal components were working under high stresses caused by transportation [8]. Besides high stresses, as it is now, train axles were working in an environment that is open to atmosphere. During working period, train axles are subjected to harsh conditions, external effect, and uncalculated mass balance. When it comes to the combination of those factors, failure was unavoidable in many cases, yet after almost 200 years of experience and knowledge, unexpected failures still occur [3]. Since the axles are subjected to cyclic loading, fatigue phenomenon takes place in terms of failure. The first known and confirmed fatigue failure of axles took place in a train accident with a major number of casualties in Versailles on 8 May 1842 due to the derailment. The cause of the accident was found that fatigue failure rooted in the front axle, which in turn, derailment of the train [9].

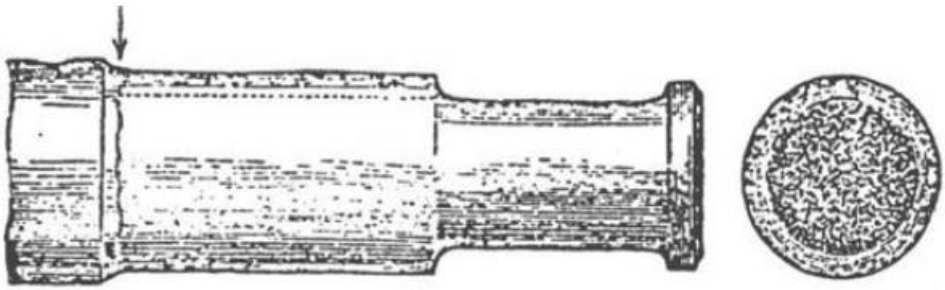

Figure 2 A representative drawing of a broken axle by Glynn [10]

Meanwhile, Stretton [11] indicated that during ten years between 1878 and 1892, 72 steel axles were failed during an in-service condition in Britain's Railways. The first extensive study of fatigue on axle components conducted by August Wöhler during 1852-1869. Wöhler developed an understanding that cyclic loading affects axle's life adversely. He performed fatigue tests where the specimens were rotated under bending stresses [12]. After a high amount of study and testing on the axle, he asserted a concept called "fatigue limit" and "S-N curves" [13].

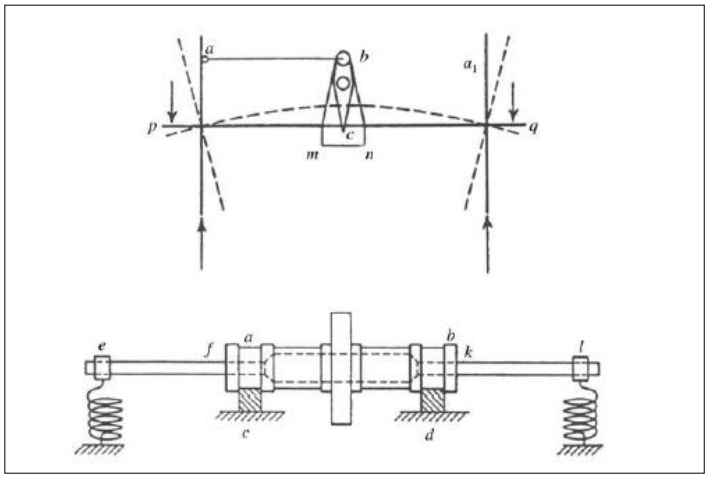

Figure 3 Upper drawing represents Wöhler's setup for fatigue testing of axles with bending stresses. The lower drawing represents the Wöhler's first fatigue testing machine working with fully-reversed bending force principle [3]

In the nineteenth century, the world focused on mass production of steel and steel components [3, 6]. Since the previous concepts were not adequate to explain the causes of failures completely, alternative theories were developed to analyze the mechanisms of failures: (e.g.) Tresca and Mises [14]. Meanwhile, World War I constituted a significant expansion of industrial production and this brought failures that had been not experienced before. These new failure mechanisms motivated scientists and engineers to develop more specific and cause-oriented concepts and theories [15]. During World War I, for example, aviation was unquestionably the greatest industry in terms of production and improvement. However, it was concluded that failures occurred in gear and crankshafts due to cyclic loading and thermal effects in long-term use [16]. Profound comprehension of fatigue failures back to 1945 when the ultrasonic testing technique was firstly introduced by Firestone [17]. This technique enabled engineers to detect cracks, inclusions, inherit deteriorations beforehand. Therefore, the probability of detection concept was born. As the probability of detection of fatigue causes was developed over time, fatigue failures remarkably decreased [18, 19].

In modern applications, "damage tolerant design" approach and "probability of detection" of material flaws by non-destructive techniques served to increase the structural reliability of the axles [20]. However, the demand for increased axle performance and reduced maintenance cost led development of axle materials, design methods, and inspection techniques [21].

The past experience with the axle failures showed that the damage tolerance and fatigue strength of the axle could be increased via metallurgical modifications in the microstructure of the axle material by heat treatment [22-24]. Furthermore, heat treatment is a cost-effective process to enhance remarkably the mechanical capabilities of steels [24]. However, high cooling rates during heat treatment include the risk of thermal cracking [20]. Additionally, thick axle sections are prone to thermal cracking and microstructural transformations due to limited quenchability of the axle material [25]. In many cases, surface hardening was utilized to constitute a compressive residual stress field on the axle surface [26]. Improvements in induction hardening by Japanese engineers during the 1960s enabled the process to be carried out to retard fretting fatigue and thermal cracking of the axles. However, surface cracking due to

rapid cooling of surface layer and formation of an extensive amount of intermetallics on the material surface may lead reduction of fatigue life [27].

A remedy for prevention of thermal cracks may be the addition of alloying elements which reduce critical cooling rate [28]. Additionally, toughening caused by alloying increase fatigue strength and the damage tolerance in many cases [20, 29]. For instance, Pendolino speed trains' axle design involves the use of novel alloys (30NiCrMoV12) with reduced cooling rates to prevent cooling cracks and protective metallic coating against fretting [20]. The coating can retard the crack initiation from material surface and thus improve fatigue life [30, 31].

One of the newest approaches "one million miles axles" concept points out the improvement in resistance against fatigue crack initiation and propagation [32]. Thus, the damage tolerance of the axle material is the key factor to maintain structural reliability during in-service failures.

Kitagawa-Takahashi application is used in critical aerospace, railway, and human body implant applications. Since those applications consist of external impacts and harsh service conditions, the life of the parts with the surface defects becomes indispensable. Beretta et al. studied on axles in the corrosive environment under high cycle fatigue loading and evaluated the corrosion cracks in accordance with Kitagawa-Takahashi analysis [33] Furthermore, scale effect become crucial for defect-free applications. Since materials may behave linear-elastic in thicker parts, the crack behavior changes. Therefore, crack propagation tests were carried out besides Kitagawa-Takahashi analysis [34]. As the urban applications have increased, more comprehensive evaluation of security risks was needed [35]. Kitagawa-Takahashi diagram was accepted as the bridge between safe-life and damage tolerance [36].

2.2. Fatigue Terminology

If part or component is subjected to cyclic or fluctuating loading, fatigue failure is inevitable. Constitutively, cyclic stress consists of 3 main parameters [37]:

- Alternating Stress
- Mean Stress
- Stress Range

Mean stress is the average of the peak and valley stresses and defines the initial stress point. Alternating stress refers to the maximum stress magnitude concerning the initial stress point. Stress range is the difference between the maximum and the minimum value [25, 37].

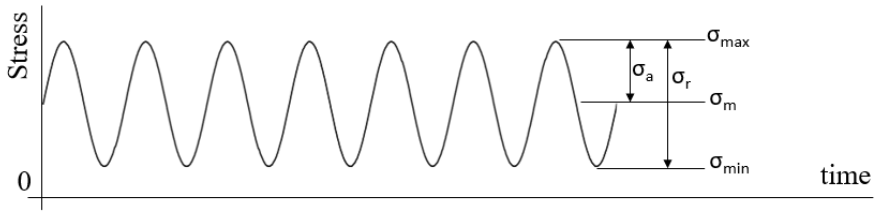

Figure 4 Constant amplitude loading diagram

$$\sigma_m = \frac{\sigma_{\max} + \sigma_{\min}}{2} \tag{2.1}$$

$$\sigma_a = \frac{\sigma_{\max} - \sigma_{\min}}{2} \tag{2.2}$$

$$\Delta\sigma = \sigma_{\max} - \sigma_{\min} \tag{2.3}$$

Regarding fatigue principle, the cyclic behavior is defined by ratio. Ratio is the correlation factor between the minimum and maximum stress or strain. The ratio is obtained by dividing minimum to maximum stress or strain value [25].

$$R = \sigma_{min}/\sigma_{max} \quad (2.4)$$

or

$$R = \varepsilon_{min}/\varepsilon_{max} \quad (2.5)$$

R=-1 represents a fully reversed condition which is obtained in rotational bending fatigue testing. In this case, mean stress or strain is zero, and every single node on the material is subjected to maximum tension and maximum compression for once in every cycle [38]. Besides R=-1, R=0 and R=0.5 are commonly used in literature and applications.

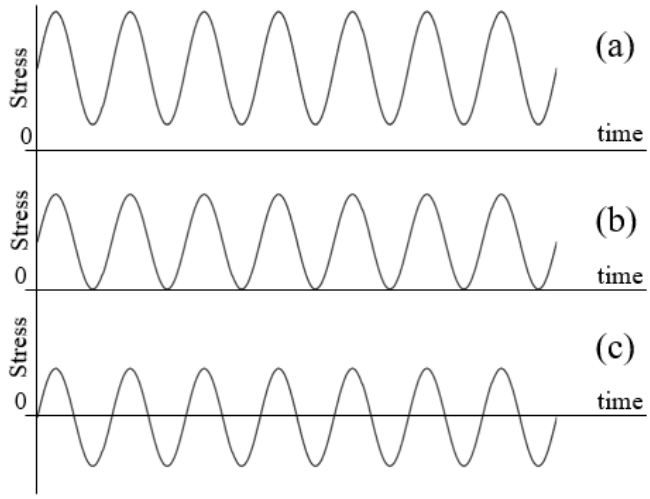

Figure 5 Basic definition of a) R>0 and b) R=0, and c) R<0 condition

2.3. Fatigue Mechanism

Fatigue mechanism may initiate whether the loading is applied above or below the yield strength. Since material may behave in terms of softening or hardening under cyclic loading, cyclic yield strength may differ from monotonic yield strength [12]. There are typically three stages of fatigue failure [12, 15, 25]:

1. A small crack nucleates on the surface of the material. Crack may nucleate by means of anything that is located in the same working environment with the material.

2. The crack begins to propagate as it reaches the propagation threshold. As the stress concentration at the crack tip increases, material starts to be exposed to elastic or plastic deformation through the crack tip. When the crack tip stress concentration reaches a critical value, long crack propagation phase initiates.
3. The crack propagates until the point where material can support the increasing loading by its thinnest cross-section, which in turn, catastrophic failure takes place.

Typical fatigue failures include three main features [38]:

- Apparent crack initiation site or sites
- Benchmarks regarding crack growth
- Apparent fracture region at the end

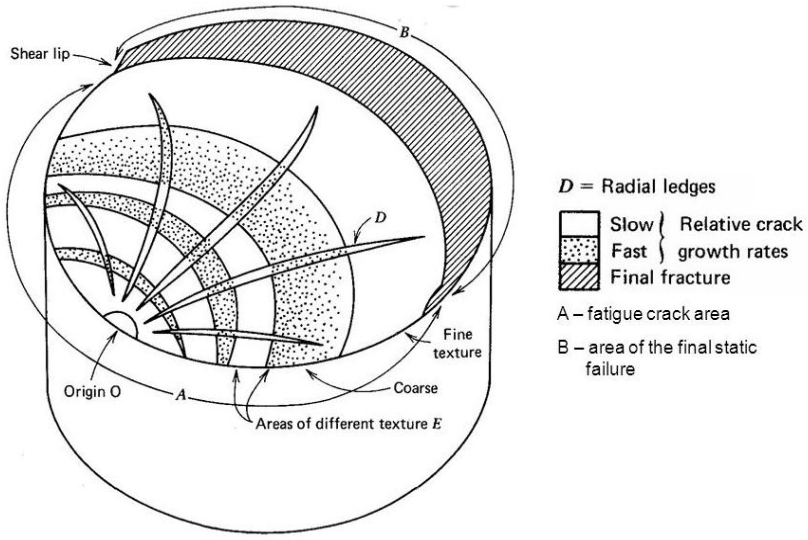

Figure 6 Representative drawing of fatigue stages. A represents the crack initiation area, B corresponds area of final failure section. D represents radial ledge which occurs in the presence of brittle fracture due to uneven crack growth [39, 40]

Crack growth rates highly depend on intermittent loading. Intermittent loading differs from continuous cyclic loading in terms of the fact that intermittent loading changes

at uncertain intervals [37]. In fatigue fracture, nucleation occurs due to slipping under loading conditions. Slipping mechanism may differ with respect to the type of loading, i.e., monotonic and cyclic.

Under monotonic loading, coarse slip bands occur since only several adjacent bands move relative to each other. However, in cyclic loading, almost all of the slip bands move in the compression, tension, or both direction [15, 38].

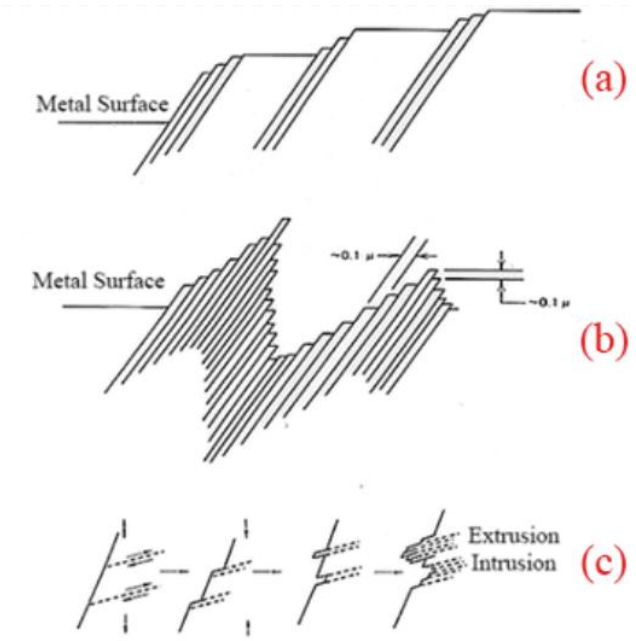

Figure 7 A representative drawing of slip bands due to (a) monotonic loading; (b) cyclic loading; (c) band movement regarding tension (extrusion) and compression (intrusion) [38]

Intrusion and extrusion movement of bands forms stress concentration among the slip bands. Stress concentration of the crack is directly related to the level of intrusion and extrusion movements. At the end of fatigue failure, macroscopic and microscopic observations of the fracture surface are required to understand the fatigue mechanism. Fracture surfaces reveal two characteristic patterns called beach marks and striations [15]. Beach marks and striations address the crack tip position and loading direction at any stage of the in-service period. That is, crack propagation path and short crack initiation phase can be readily determined by observing the crack surface. Both beach

marks and striations expand from the crack initiation point in semi-circular regime in most cases [32, 41, 42]. If there is no multi-crack initiation the fatigue fracture surface, beach marks and striations show appearance similar to the consecutive waves in the loading direction. Beach marks occurring due to fluctuating, and intermittent loading can be observed by unaided eye, whereas striations can only be observed by SEM. Since they are micron-scaled patterns, striations indicate the position and propagation path of the crack tip after every cycle [43]

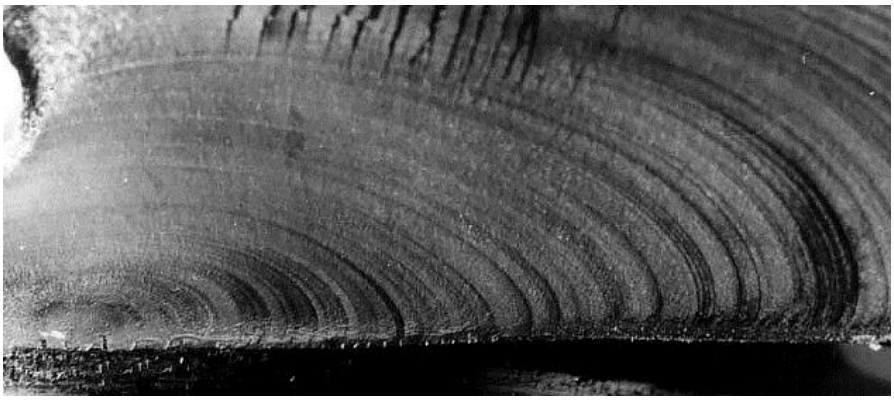

Figure 8 Fatigue benchmarks on the crack surface [44]

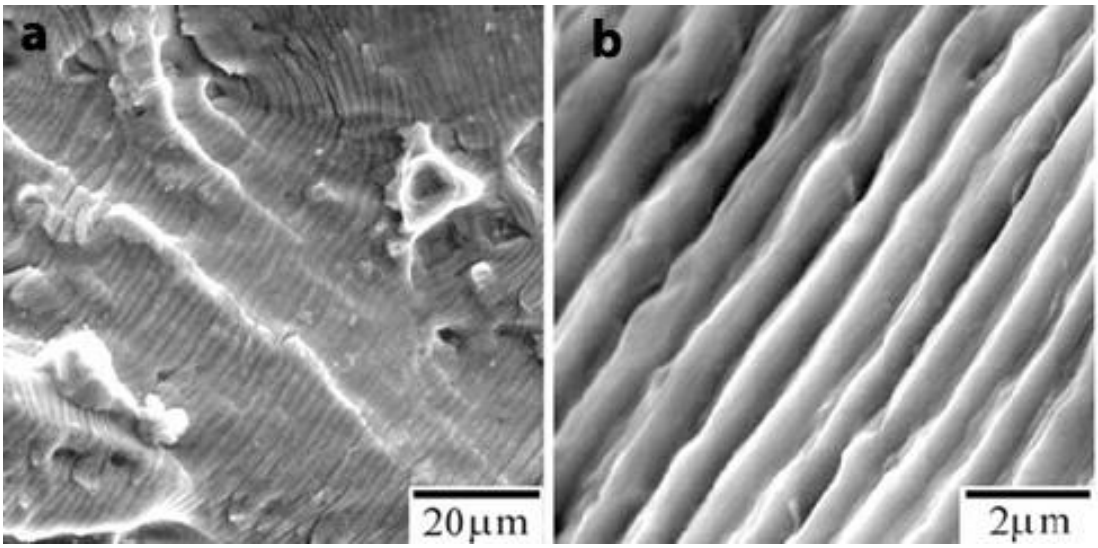

Figure 9 Typical striation formation [45]; a) fatigue originated striations due to constant amplitude loading; b) a higher magnification image

In some cases, multi-crack initiation may occur due to loading, surface condition, temperature, etc [46]. During cyclic loading, cracks may initiate due to poor

machining, unbalanced loading, inherit inclusions in several points. At the same time, as the cyclic loading continues, cracks start to grow and propagate. Cracks tend to propagate in a direction parallel to the loading direction. After a while, they join together at some point leading to catastrophic failure [12, 47]. Depending upon the loading conditions, fatigue mechanism may differ in terms of morphological features of the fracture surface [41, 43].

The typical loading conditions [38] can be given as:

- Tension-Compression
- Reversed Bending
- Rotational Bending
- Unidirectional Bending

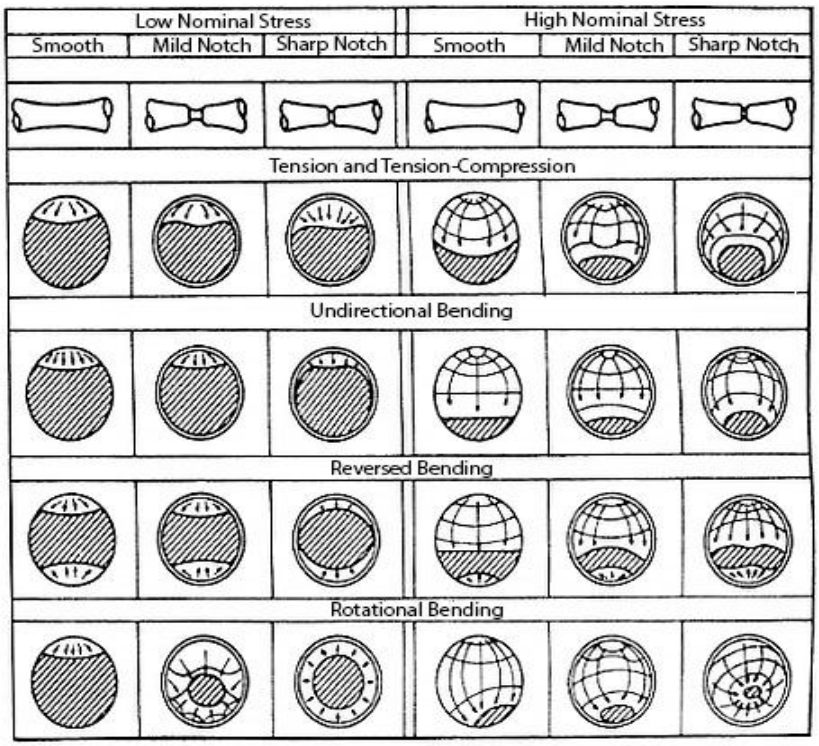

Figure 10 Different surface morphologies due to fatigue failure for axial and bending loading (rearranged) [42]

2.4. Total Life Approaches

The total fatigue life can be defined by two approaches: Stress-life and strain-life. The difference between stress and strain approach occurs at the point of loading spectrum. The type of loading is determined depending upon the design requirements and working conditions. Fatigue design consists of six main parameters which are geometry, history of loading, environment, design criteria, material properties, and effect of processing [38, 41].

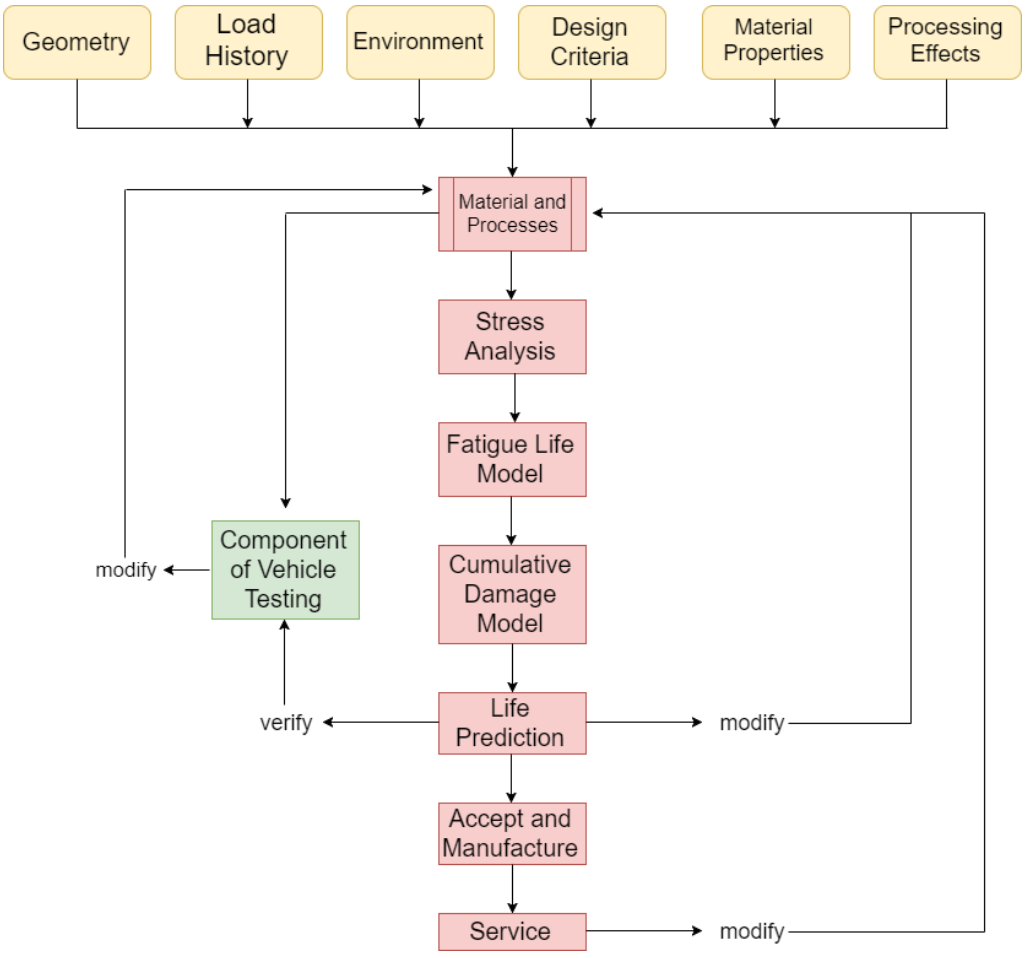

Figure 11 Flow diagram of fatigue design (rearranged) [38]

2.4.1. Stress-Life Approach

Stress-life approach covers the concept of constant cyclic loading in the elastic deformation regime which was introduced by Wöhler [12]. Wöhler performed fatigue test on train axles to understand the relationship between stress and the cycles to failure point. He concluded that the fatigue phenomenon is no longer valid at a stress value (endurance limit) where the material does not fail. It means that the infinite life of the component at specific stress level is called "endurance limit" [48]. Endurance limit is only valid if the material is in totally defect-free condition. This concept was commonly used in fatigue testing and analysis if the component to be tested was under low-amplitude cyclic loading. If the fatigue testing is performed with constant loading, it is called "high cycle fatigue" (HCF) [12, 38]. Stress-based fatigue testing consists of four testing set-ups [38]:

- Bending Test
- Rotating Bending Test
- Uniaxial Tension-Compression Test
- Tension-Tension Test

S-N curves are formed at the end of the number of high cycle fatigue tests. S-N curve is a diagram illustrating the relationship between stress and the number of cycles to failure.

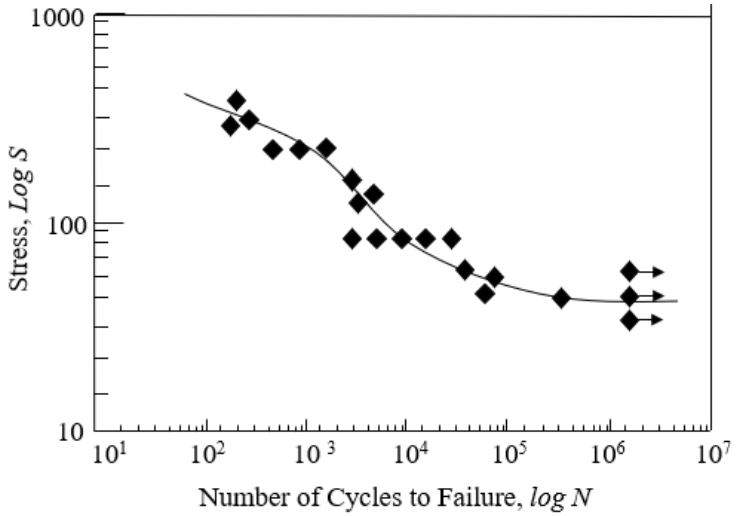

Figure 12 A typical S-N curve. S_f represents endurance limit

In most cases, fatigue life decreases as the amount of plastic deformation increases. The value of endurance limit is considered $30-35\%$ of tensile strength in most cases for steels up to at least 10^7 cycles [49, 50]. Crack initiation period is the pre-phase before crack propagation. The crack starts to propagate when it surpasses propagation threshold that is specified for each crack length. Once it reaches its threshold value, it begins to propagate until failure. The loading amplitude determines the propagation rate under such conditions.

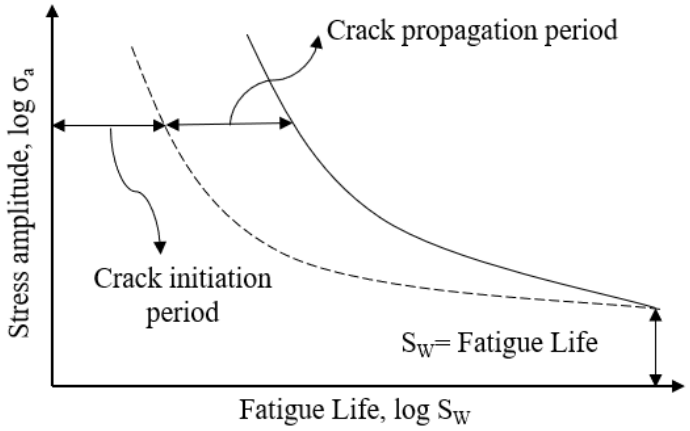

Figure 13 Crack initiation and failure phases (rearranged) [51]

2.5. Fracture Mechanics

Fracture mechanics is an advanced method to evaluate the crack growth rate, fracture toughness, and the relationship between flaw size and stress levels. Fracture mechanics covers the "fitness-for-service" concept and brings reliable approaches to material design [15, 52]. The reliable approach consists of two main parameters which are stress level and flaw size.

Fracture toughness is the resistance of the material against crack propagation [15, 44, 53]. It is a key parameter for such applications designed by the fitness-for-service concept. Since adverse effects such as unbalanced heating or loading, corrosion, and external damages can be readily formed in an unpredictable environment, flaw formation is the only parameter is to be considered as a potential problem. Flaws may occur as cracks, inclusions, voids, inherit discontinuities, welding defects, etc. as shown in Figure 14. There is different damage mechanism for each flaw type owing to the fact that they are shaped in different forms, sizes, and morphological properties.

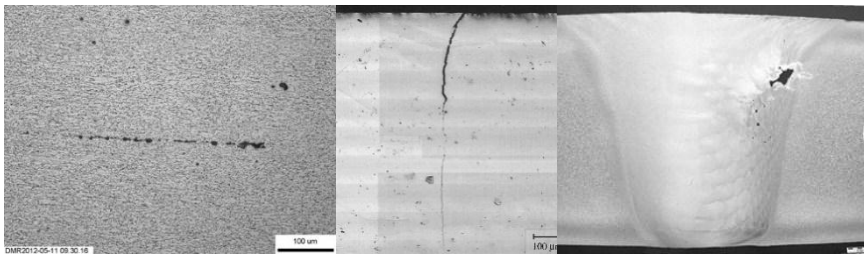

Figure 14 Typical flaws encountered in applications: (from left to right) Inclusion, crack, and voids [54, 55]

Fracture toughness of a material is defined by the stress intensity factor, K. Stress intensity factor determines the fracture toughness of materials in three different fracture modes illustrated in Figure 15. These fracture modes can be indicated as:

- Mode I (Tensile Fracture)
- Mode II (Shearing Fracture)
- Mode III (Tearing Fracture)

Mode I is the fracture mode where stress is perpendicular to the crack plane surface. This mode is the most commonly encountered mode in applications. Mode II is expressed as shearing mode as the stress is parallelly applied to the crack surface and perpendicular to the crack propagation front. Mode III is the tearing mode where stress is not only parallel to the crack plane surface but also to crack propagation front [12, 52].

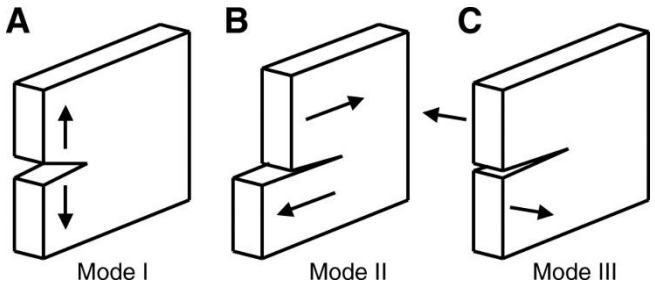

Figure 15 Modes of fracture [56]

Critical stress intensity factor (2.7) consists of three diversified parameters which are crack size, stress, and geometric factor for each specimen type.

$$K_C = \beta\sigma\sqrt{\pi a} \tag{2.6}$$

where σ is critical stress for crack propagation and failure in MPa; a is the crack length in meters; β is the dimensionless geometry factor.

K_{IC} is the fracture toughness of the material where crack tip requires to perform a failure. K_{IC} is where the brittle fracture occurs due to the plane-strain condition. K_I is the stress intensity factor representing specific value for each stress level. K_I is a thickness dependent parameter and as the thickness increases, K_I decreases until it reaches K_{IC} value at the plane-strain condition [12, 15, 50]

2.5.1. Linear Elastic Fracture Mechanics

Linear Elastic Fracture Mechanics (LEFM) is a fracture concept defined by stress intensity factor (SIF) and represent as a parameter of stress and flaw size. LEFM is basically based on elasticity theory. It was firstly introduced by Griffith [57] and developed by Irwin [58] to comprehend the concept of short crack behavior and crack propagation in elastic structures. Griffith proposed that potential energy of the material can create new crack surfaces as it increases. Brittle materials exhibit elastic deformation at the crack tip, and the critical condition for this approach is given in (2.7).

$$\frac{\partial}{\partial c}[U_E - U_S] = 0 \tag{2.7}$$

where U_E is the energy required to create new cracks per unit thickness; c is the half of the crack length; and U_S is the elastic surface energy under tensile loading per unit thickness (2.9).

$$U_E = \frac{\pi\sigma^2 c^2}{E} \tag{2.8}$$

$$U_S = 4cT \tag{2.9}$$

where T is the surface tension in case of breaking atomic bonds while crack formation and equals $1.97 \times 10^{-8} E\alpha_a . \alpha_a$ represents atomic spacing in Angstroms. The equation that defines the crack extension force i.e., energy release rate in half of a center crack in an infinite plate is given in (2.10)).

$$\frac{\pi\sigma^2 c}{E} = 2T \tag{2.10}$$

where σ is applied stress during loading. The energy release rate is used as energy balance approach in brittle materials, however, it is only applicable for cases where

final failure is a result of monotonic loading. It cannot be applied to the materials that are subjected to cyclic loading. Therefore, stress intensity factor is a crucial parameter to analyse the crack behavior under cyclic loading. Irwin concluded that G and K approaches can be linked together to understand the relationship between crack behavior under monotonic and cyclic loading conditions. This relationship is indicated in (2.11)).

$$G = \frac{\pi\sigma^2 c}{E} = \frac{K^2}{E} \tag{2.11}$$

LEFM can be applied to all types of materials in case of all conditions required for LEFM is met.

2.5.2. Small Cracks

Small cracks may originate from corrosion pits, material inhomogeneities or surface flaws caused by the mechanical effect. Short crack behavior may be examined in three stages: microstructurally short cracks, physical short cracks and long cracks [59, 60]. Size of microstructurally short cracks is comparable to the grain size of the material. Microstructurally short cracks constitute an interphase where the microcrack is initiated but not propagated. Physically short crack describes the stage at which the cracks begin to propagate [61]. The growth rate in the short crack regime is higher than that in the long crack propagation [62] shown in Figure 16. The mathematical approach to short cracks indicates that the propagation limit only can be overreached if the stress corresponding to the fatigue limit of the material is reached at the crack tip [63].

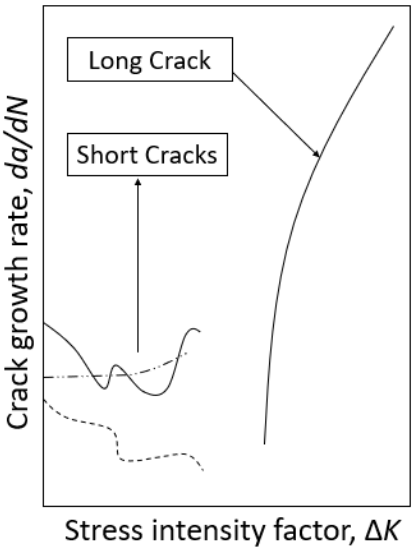

Figure 16 A representative drawing of short crack instability and comparison of short and long cracks

2.5.3. Long Crack Propagation

Long crack propagation is defined as stable propagation. As the cyclic loading continues, fatigue crack tends to propagate through the grains. Therefore, crack becomes independent from the effects that may create instability. Crack propagation occurs in a path determined by the material, load, and environmental conditions [38, 46].

Figure 17 The primary steps of a fatigue failure

Propagation direction can constitute itself in two distinctive paths: transcrystalline and intercrystalline.

In most cases, the crack tends to grow across grain boundaries, in other words, transcrystalline direction. However, intercrystalline propagation can be observed through grain boundaries regarding loading, material, and environmental conditions.

As the crack initiates, it begins to propagate at different crack growth rates at a different stage of propagation in the sequel [38].

There are several factors that directly affect the crack growth rate, and the most important ones are stated as:

- Stress intensity range, ΔK
- Stress intensity ratio, R
- Stress history

As the stress intensity and the stress intensity ratio increases, crack growth rate increases as well. On the other hand, if the material is previously exposed to fluctuating and unbalanced stresses, it may affect the hardening or softening mechanism of the material.

Crack propagation consists of 3 stages: stage I (shear stage), stage II (tensile mode stage), and stage III (final fracture stage) [12, 38, 41, 64] given in Figure 18.

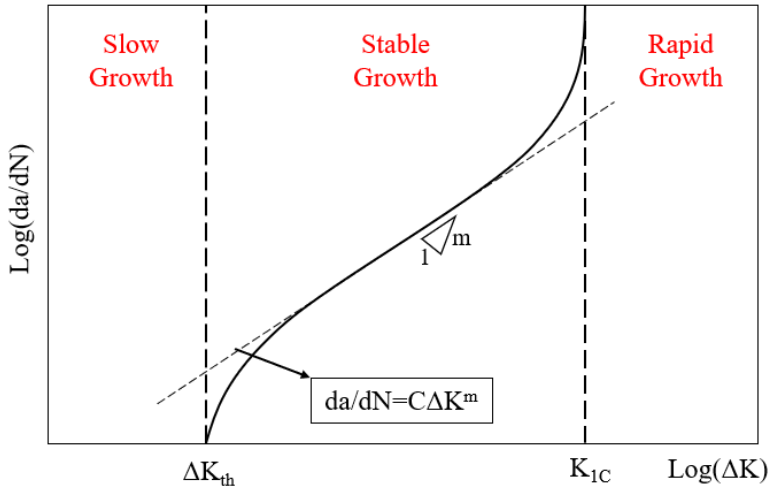

Figure 18 Stages of crack propagation

Stage I is called "short crack propagation," and crack propagates along the shear stress planes directly. Propagation continues in instability condition among shear planes until the crack is decelerated by a grain boundary, inclusion or a microstructurally formed barrier [38, 60]

Stage II is called “long crack propagation.” In this stage, as the K increases, cracks start to propagate in different directions rather than along 45° shear plane, moreover, at different crack propagation rates. Crack propagation rate, da/dN, is obtained in this stage owing to the correlation between crack size, a, and the number of cycles, N. Crack propagation rate depends on ΔK and stress ratio R, however, the dependency of rate is not an important parameter in stage II. Paris and Erdogan [65] postulated that material’s fatigue life in terms of propagation rate can be estimated by two material constants: C and m. m is known as “Walker constant” is used to correlate the mean stress and stress amplitude [37]. In stage II, the fatigue life can be directly estimated by Paris-Erdogan Law [65-67] is given (2.12)

$$\frac{da}{dN} = C\Delta K^m \tag{2.12}$$

where ΔK represents stress intensity factor range, and da/dN signifies crack growth per number of cycles to failure.

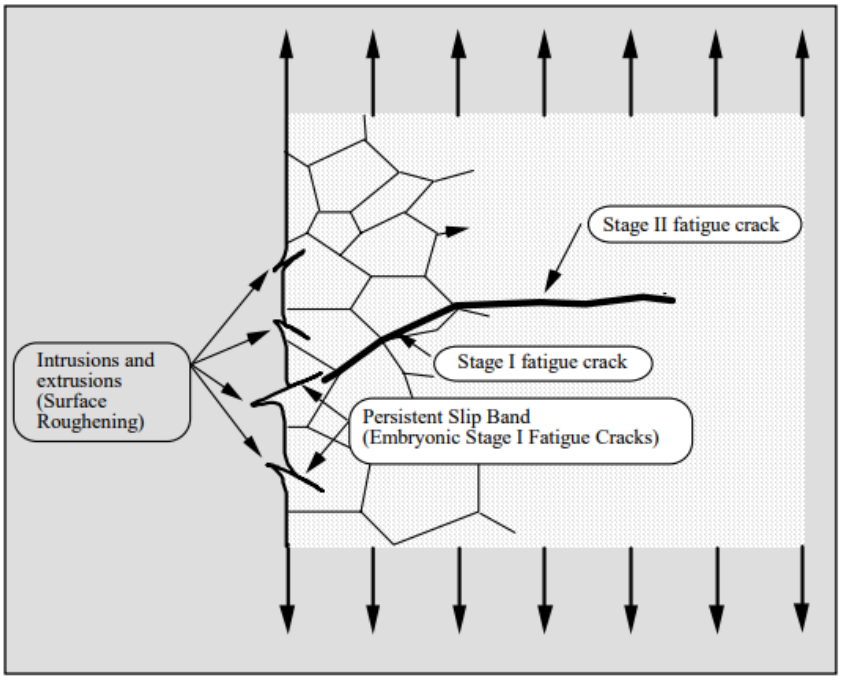

Figure 19 Schematic representation of fatigue crack growth in stage I and II [64]

Striations are commonly visible at stage II for pure and ductile metals [38]. Laird [68] proposed that striation formation require varied types of loading during fatigue mechanism. Since every single cycle forms micro or nano striations at this stage, formation mechanism becomes crucial. Striation formation mechanisms can be given as:

- No load formation
- Tensile load formation
- Maximum tensile load formation
- Load reversion formation
- Compressive load formation

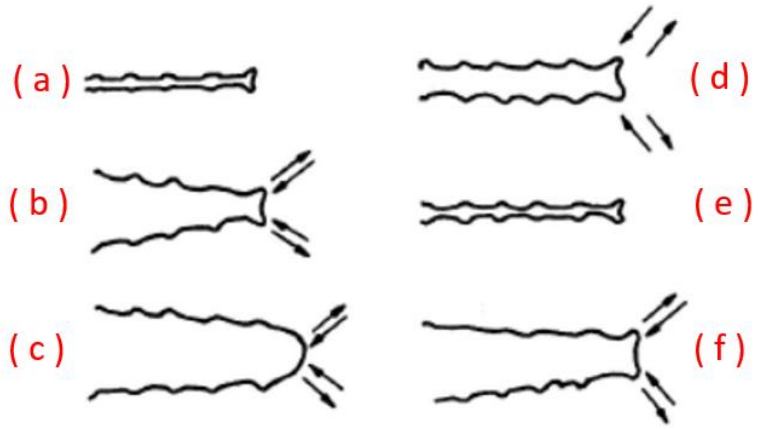

Figure 20 Striation formation mechanisms a) no load; b) tensile loading with small amplitude; c) peak tensile loading; d) reversal loading; e) peak compressive; f) maximum tensile loading [12, 64]

At stage III, unstable crack growth occurs. Crack growth rate increases as cracks approach the final fracture point. This stage is mainly controlled by K_C or K_{IC}, however, mean stress, loading type and microstructure can affect the control mechanism, too. As the stress intensity factor, SIF, at the crack tip reaches K_{IC} value, failure occurs in brittle manner for most of the cases [12, 15, 67].

2.6. Elastic-Plastic Fracture Mechanics

Contrary to LEFM, elastic-plastic fracture mechanics (EPFM) is a fracture approach which supports the concept of plastic deformation and yielding in big scale during crack propagation at the crack tip. Wells [69] and Rice [70] developed the concept suggested by Griffith in terms of plasticity due to the fact that Griffith's theory covers elastic deformations and brittle fractures. [15]. If the material behaves in ductile manner, the crack propagates in a path where it can create plastic zones at the crack tip [50, 71]

EPFM is expressed regarding two different sub-approaches: Crack Tip Opening Displacement (CTOD) and J-Integral
Even though CTOD and J-Integral are represented in terms of EPFM, J-Integral is used to determine the energy dissipated during crack propagation and CTOD is used to obtain displacement required for propagation [72].

2.6.1. Crack Tip Opening Displacement (CTOD)

CTOD is the required displacement on the crack tip for the crack to propagate. This approach is preferred in materials when plastic deformation is observed at the crack tip. It was first introduced by Alan Wells to define the mechanism of displacement on the crack tip in plasticity [73, 74].
CTOD is based on the 45° plane lines where the plane lines and crack extensions are intersected [12] as illustrated in Figure 21.

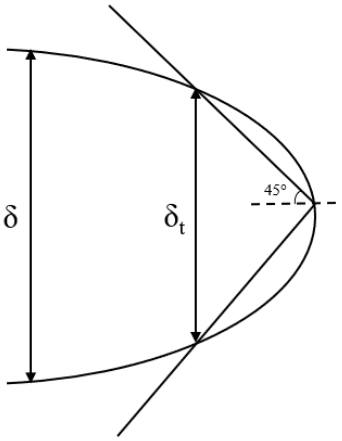

Figure 21 Crack tip opening displacement, δ_t (rearranged) [75]

The relationship between CTOD and SIF can be formulated by using Dungale's plastic zone size approach [76] given in ((2.13)):

$$\delta_t = \frac{K_I^2}{E\sigma_y} = \frac{G_I}{\sigma_y} \tag{2.13}$$

where δ_t is the CTOD at the crack tip; K_I is the stress intesity factor in mode I loading; E is elastic modulus; σ_y is the yield strength obtained under monotonic increasing loading; and G_I the is energy release rate obtained in mode I loading [15].

2.7. Plane Stress and Plane Strain Conditions

When the material is subjected to increasing loading, plastic deformation occurs as the applied stress exceeds the yield strength. In this case, the material can be plastically deformed in the direction of free surface with 45° [12]. If the material can be plastically deformed, it indicates that the material is relatively thin, and fracture takes place in a ductile manner. This condition is called "plane-stress." However, if the material is relatively thick and the crack tip is away from the free surface, it cannot be plastically deformed. If there is negligible or no plastic deformation, this condition is called "plane-strain" [49, 77]

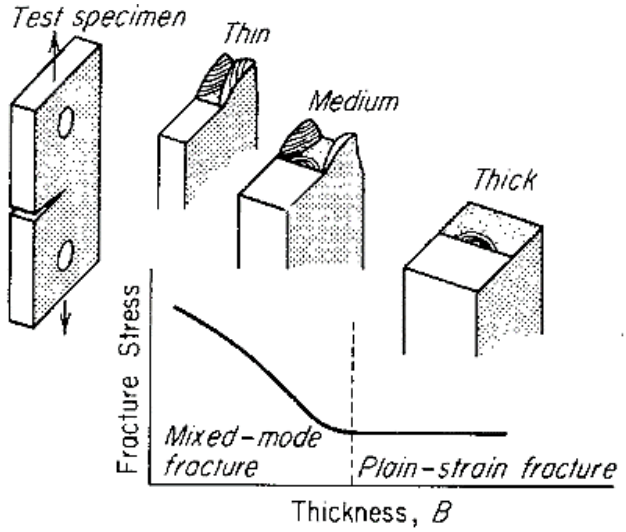

Figure 22 Effect of the specimen thickness on fracture toughness [49]

Plane strain condition prevails regarding fracture toughness when

$$B \geq 2.5\left(\frac{K_{IC}}{\sigma_Y}\right) \tag{2.14}$$

where B is the material's thickness (mm) and σ_Y is the yield stress (MPa). Plane stress condition is obtained when there are distinct shear lips on the fracture surface of the material [49].

CHAPTER 3

EXPERIMENTAL PROCEDURE

3.1. Experimental and Analytical Approach

The presented work contains a comparative investigation of different conditions of a typical railway vehicle axle material regarding microstructural and mechanical properties. The material conforms to the specifications of EN 10083-3 [78] as 34CrMo4 or ASTM A29/A29M [79] as AISI 4135. Fatigue performance of such material conditions is the main focus of the study.

The specimens were sectioned from an axle, which was received from Turkish State Railways. Optical emission spectral analysis of several spots on the axle confirmed that the elemental constituents of the material confirmed the specifications [78, 79]. However, Mn was found to be lower, and P was higher than those specified in the standard limits.

Table 1 Specified weight fractions of the elements in the axle (% weight)

Material	C	Cr	Mn	Mo	Si	P	S
Laboratory Analysis	0.31	0.91	0.39	0.21	0.28	0.04	0.03
EN 10083-3 [78] 34CrMo4	0.30-0.37	0.90-1.20	0.60-0.90	0.15-0.30	0.40 (max.)	0.03 (max.)	0.04 (max.)

A schematic representation of the microstructural and mechanical characterization and data analysis procedure is given in Figure 23. Reference standards and the number of specimens are listed in Table 2.

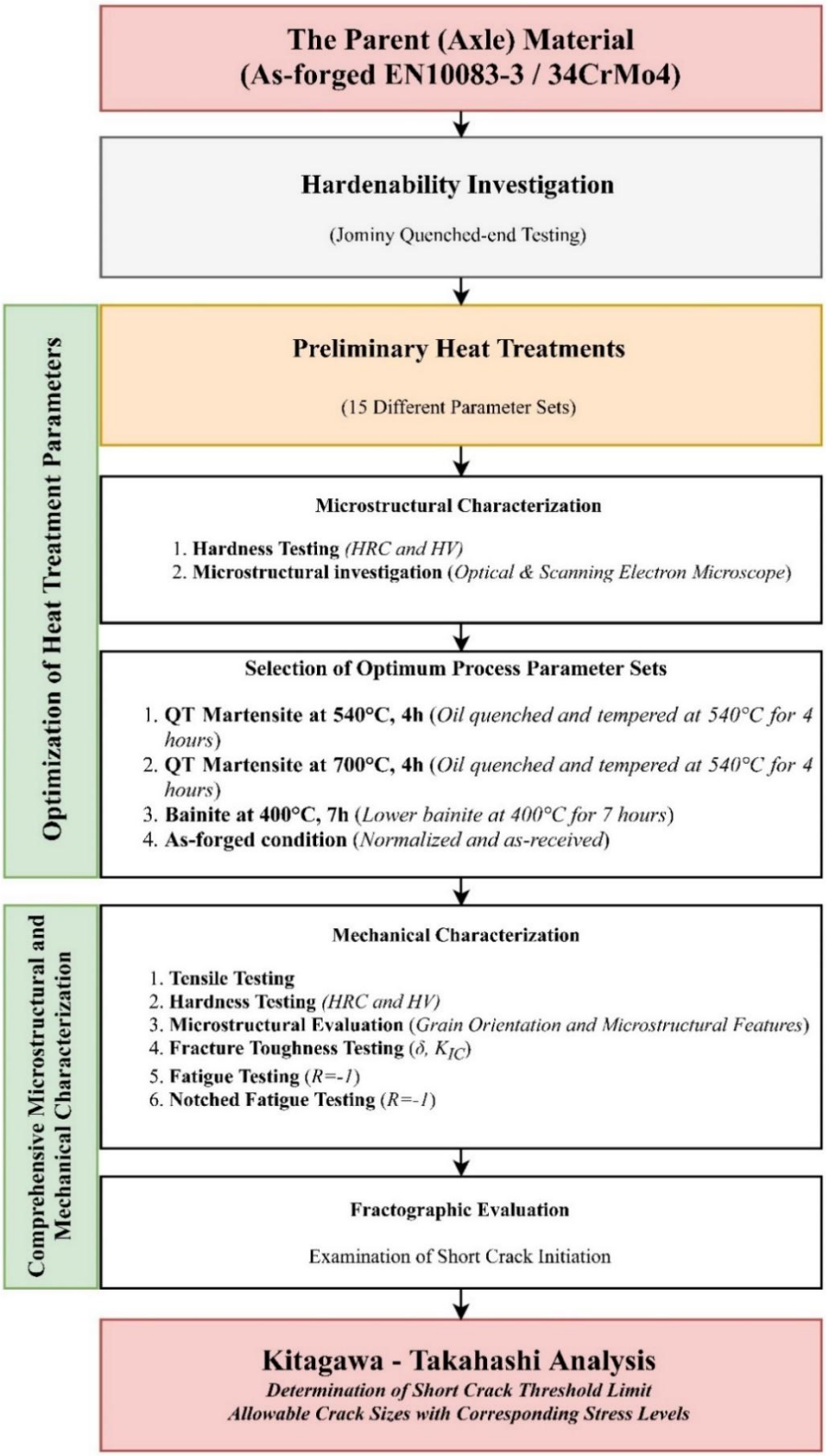

Figure 23 Flowchart of experimental and analytical processes

Table 2 A comprehensive overview of the test plan

Tests	Reference Standards	Number of Specimen	Section
Spectral Analysis	ASTM E3-11	2	0
Hardness Testing	ASTM E18-17e1 ASTM E92-82 ASTM E140-02 ISO 6508-1	40	3.3.2
Jominy Quenched-end Testing	ASTM A255-07 ISO 642	1	0
Tensile Testing	ASTM E8/E8M ISO 6892-1	10	3.3.1
Fatigue Testing	ASTM E466-15 ISO 1143 ISO 12107 ISO 1099	63	3.3.4
Fracture Toughness Testing	ASTM E1820 ASTM E399 ISO 12135 ISO 12737	8	3.3.3
Notched Fatigue Testing	ASTM E466-15 ISO 1143 ISO 12107 ISO 1099	92	3.3.5

3.2. Material Characterization and Verification

Elemental constituents of mechanical properties of AISI 4135 steel are specified in EN 10083-3 [78]. These specifications also match ASTM A29/A29M [79] AISI 4135. Spectral analysis specimens were prepared in accordance with ASTM E3-11 [80] and examined by Optical Emission Spectrometer (OES). The chemical composition of as-received material was determined to be shown as in Table 1.

The specimens were then subjected to metallographic examinations. Emery papers with a grade of 240, 400, 800, and 1000 were used respectively for grinding process at the first step. Polishing process was performed with diamond polishing paper to prepare specimens for the micro-examination at the latter step. Specimens were etched with 2% Nital and LaPera solution and subsequently cleaned with alcohol to remove the solution from the surface. The chemical composition of the solution is given in Table 3. Surfaces were examined under Olympus Optical Microscope and METU MetE NOVA NANOSEM 430 Scanning Electron Microscope (SEM) after metallographical preparation of specimens.

Table 3 Reagents employed during metallographic examinations

Reagent	Composition	Application	Use
2% Nital	- 2 wt% Nitric Acid (HNO_3) - 98 wt% Ethanol (C_2H_6O)	**Etching:** 10 sec **Polishing:** 1 μm diamond colloidal paper	Microstructural Examination and Evaluation
LaPera	- 1 wt% Sodium-metabisulfite $Na_2S_2O_5$ - 4 wt% Picric acid $C_6H_2(NO_2)_3OH$ - 46 wt% Ethanol (C_2H_6O) - 49 wt% Demineralized water	**Etching:** 10 sec **Polishing:** 1 μm diamond colloidal paper	Bainite / Pearlite / Ferrite / Cementite / Martensite / Retained austenite

3.2.1. Investigation of Hardenability

34CrMo4 (AISI 4135) was analyzed in terms of its heat treatment capability and properties. It is mostly used as quenched and tempered condition due to its high hardenability. Its low-carbon content results in high formability and can be readily modified by heat treatment. It is usually quenched in oil to prevent thermal cracking.

Jominy quenched-end tests were performed and evaluated according to ASTM A255-07 [81]. Specimen configuration and set-up were adapted from this standard are shown in Figure 24.

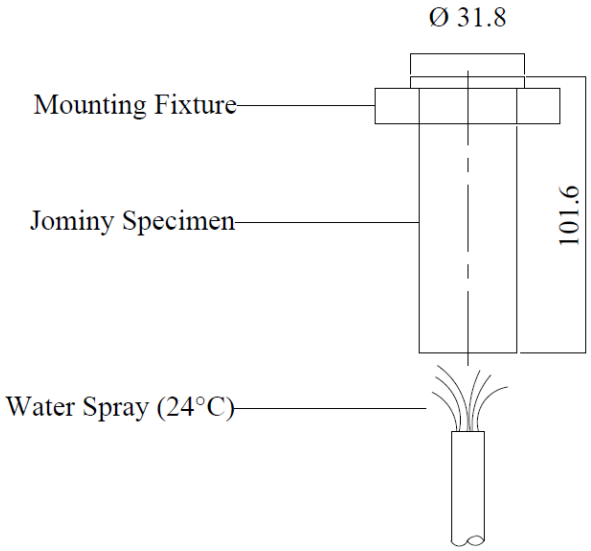

Figure 24 Jominy quenched-end test specimen configuration and set-up

The specimen was held at 870°C for 30 minutes to obtain fully-austenite phase through the specimen. The heated specimen was rapidly placed into the Jominy quenched-end test set-up where water spray at 24°C was directly applied to the bottom of the specimen for 10 minutes.

The specimen was removed and cut by its cap to get a plain surface for hardness measurement in accordance with ASTM E18-17e1 and ASTM A255-07 [81, 82]. Hardness measurement was performed along the flat surface at certain intervals, and hardness profile diagram was constructed regarding hardness and distance from the quenched end.

3.2.2. Heat Treatments

Heat treatment of AISI 4135 steel was specified in accordance with ASM Heat Treatment Handbook [83, 84]. The specimens were heat treated in HI Industry Heat

Treatment Furnace, and a salt bath with high-temperature range are given in Figure 25.

Figure 25 Conventional heat treatment furnace and salt baths with high-temperature range (from left to right)

Heat treatment steps and temperatures were determined by Jmat Pro software. Jmat Pro gives an accurate map for heat treatment steps, TTT, and CCT diagrams. The results were compared and verified with the those in the Atlas of Time-Temperature Diagrams for Irons and Steels [85]. The parameters required for heat treatment mapping are;

- Chemical composition
- Grain size
- Austenitization temperature

Austenitization temperature was applied as 870℃ where the AISI 4135 steel is in fully-austenitic phase. Quenching steps were performed in oil due to prevent thermal cracks on the specimen. Lower bainite was obtained in the salt bath at 400℃. Hardness measurement was conducted at the end of each heat treatment and the results compared with those in the EN 10083-3 and ASM Atlas of Time-Temperature Diagrams for Irons and Steels [78, 85].

3.3. Mechanical Characterization

A series of mechanical tests were carried out according to related ISO and ASTM standards.

3.3.1. Tensile Testing

The tensile test was performed according to ASTM E8/E8M and ISO 6892-1 [86, 87]. Specimens were sampled in the longitudinal direction from the axle. Tensile tests were performed on the Instron 5582 30kN and Zwick 250kN static testing machines are shown in Figure 26. Tensile tests were carried out at room temperature using both 0.02 mm/mm and 1.8 mm/min strain rate after yield point.

Figure 26 Zwick 250kN tensile testing machine

The specimen configuration is indicated in Figure 27 where;

- d_0: Initial diameter at the thinnest section of the specimen
- L_c: Minimum parallel length
- L_0: Gauge length

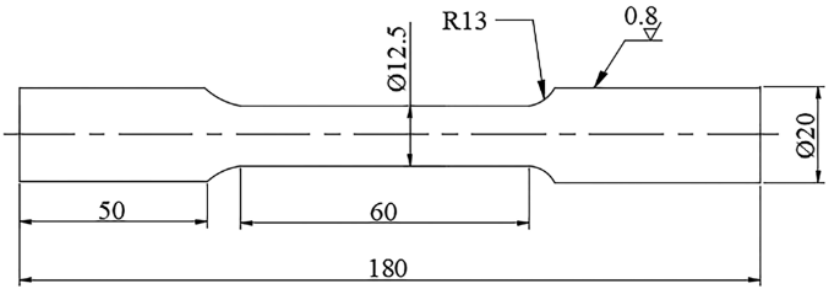

Figure 27 Tensile test specimen configuration

At the end of a series of tensile tests, true and engineering stress-strain curves were obtained.

3.3.2. Hardness Testing

Hardness tests were carried out with not only dummy specimens but also tensile and fatigue specimens in order to be sure equivalent hardness values were obtained. Hardness testing was conducted on Universal Emco M4U-025 in accordance with ASTM E10 and ISO 6507-1 (Figure 28). A single diamond indenter with a rounded 0.2 mm radius tip is used to measure the hardness of the material.

Figure 28 Hardness measurement equipment

3.3.3. Fracture Toughness Test

Since some microstructural configurations behave in a ductile manner in the plane – strain conditions, measuring crack mouth opening displacement (CMOD) was required. Both K_{IC} and CTOD tests were carried out to evaluate fracture toughness of material by fracture toughness testing in accordance with ASTM E399, ISO 12135, and ISO 12737 [88-90]. Fracture toughness test was performed on Besmak 100kN three-point flexural bending machine with a speed rate of 0.7 mm/mm. The specimen configuration is given in Figure 29 where;

- W: Width of the specimen
- B: Thickness of the specimen. It is generally used as the half of W $(2B = W)$
- a = Initial notch size (includes pre-crack)

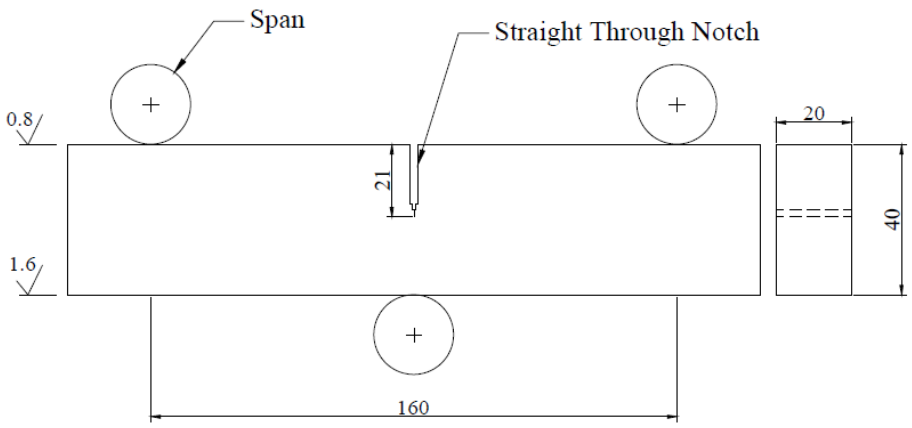

Figure 29 A representative drawing of fracture toughness test specimen

Specimens with 20 mm thickness (B) and 40 mm width (W) were used. Initially, specimens were machined to create an initial notch by "Wire Electric – Discharge Machining" (WEDM). It is the most efficient method when low residual stress is desired. This process was performed under the distilled water in order to create an isolated environment. The wire was constantly fed with electricity so that wire can be discharged whenever it touches to the specimen.

Pre-cracking was done by sinusoidal cyclic loading with R=0.1 to simulate fatigue crack growth prior to fracture toughness test. The pre-crack load was chosen as a load that does not exceed 80% of the predicted K_{IC} value to prevent overloading. Pre-cracking process was carried out on MTS 810 servo-hydraulic testing machine under tension – tension loading with R=0.1 shown in Figure 30.

Figure 30 MTS servo-hydraulic test machine

Fracture toughness tests were performed at room temperature. Crack mouth opening displacement (CMOD) data was recorded by clip-on gages. Load versus CMOD graphs values were drawn in accordance with ISO 12135 [90]. Then the K_{IC} and K_Q values were determined by using own excel VBA codes. Fracture toughness data was characterized in terms of K_{IC} and $CTOD$ testing. K_{1C} (3.1) and CTOD (3.2) values were calculated in accordance with three-point bend specimen requirements [90, 91].

$$K_Q = \frac{F_Q S}{\sqrt{B^2} W^{3/2}} f\left(\frac{a}{W}\right) \tag{3.1}$$

$$\delta_O = \left[\left(\frac{S}{W}\right)\frac{F}{\sqrt{B^2W}}g\left(\frac{a_0}{W}\right)\right]^2\left(\frac{1-v^2}{2R_{p0.2}E}\right)+\frac{0.4(W-a_0)}{0.6a_0+0.4W}V_p \qquad (3.2)$$

where K_Q is toughness value at a given stress, F is the force, S is bending span, B is specimen thickness, W is specimen width, $f\left(\frac{a}{W}\right)$ is a function of K_Q, δ_O is CTOD, $g\left(\frac{a_0}{W}\right)$ is a function of δ_O, v is Poisson's ratio, $R_{p0.2}$ is yield strength, E is elastic modulus, and a_0 is initial crack length.

3.3.4. Fatigue Testing

Fatigue tests were performed in accordance with IS0 12107 and ISO 1099 [88, 92] using rotational beam fatigue machine with R=-1 tension-compression loading (Figure 31).

Figure 31 Rotational beam fatigue testing equipment

Specimens were prepared in the form of hourglass geometry where;

- d: Diameter at the thinnest section of gage where stresses are maximum
- D: Diameter of the end of the specimen

- F: Applied force
- L: Force arm length

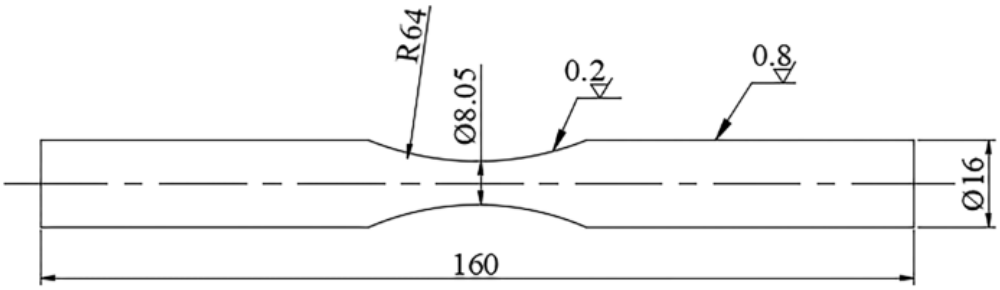

Figure 32 Technical drawing of fatigue specimen

Grinding and polishing steps were done carefully to eliminate the early fracture since the poor surface finish (i.e. high surface roughness) has an adverse effect on fatigue life as illustrated in Figure 33.

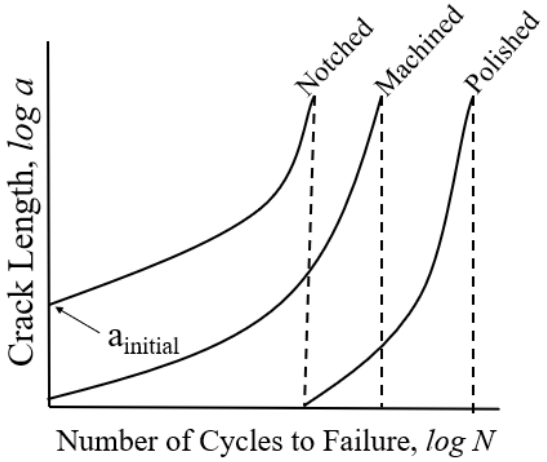

Figure 33 Surface finish effect on fatigue life

Stress and moment distributions on the gage section of specimens with respect to 2-point loading were given in Figure 34.

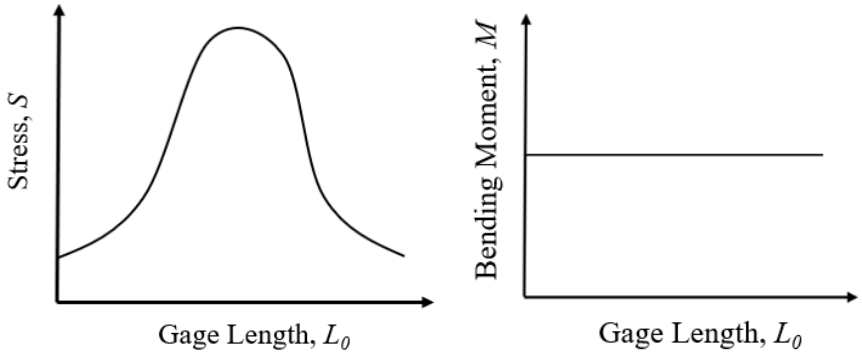

Figure 34 Corresponding stress and bending moment distribution on fatigue testing equipment [92]

Fatigue limit was accepted as 5 million cycles without failure and named as "run – out". Fatigue data was evaluated by "Staircase Method" where stress ranges and intervals were determined with reference to previous stress and test specimen condition whether it is failed or not at the end of each fatigue testing.

Staircase method was explained in detail in [88]. Staircase method consists of stresses that are determined with a considerable interval limit. In this study, stress interval was accepted as 30 MPa. The first stress is commonly given as $0.6 \times \sigma_y$ (σ_y: yield strength), and then the stress is changed in accordance with the number of cycles to failure (Figure 35).

Stress (MPa)	1	2	3	4	5	6	7	8	9	10	11	12
480												
450						**X**						
420			**X**		**O**		**X**					
390		**O**		**O**				**O**				
360	**O***											
X: Broken				O: Run-out				O*: Not Counted				
Parameter	**Test Sequence (Modified Staircase)**											
i	1	2	3	4	5	6	7	8	9	10	11	12
S_i, MPa	390	420	390	420	450	420	390	420				
Event	**O**	**X**	**O**	**O**	**X**	**X**	**O**	**X (hyp)**				
μ_Y, MPa	412.50											

Figure 35 The determination of stress map and the average value of a specimen according to Staircase Method

i is the number of specimens, S_i is the ist given stress level, *event* represents the failure or run-out specimen, μ_Y is the average value, *hyp* is hypothetically given value at the end.

At the second step, valid stress values in terms of the results of broken samples are evaluated by modified Staircase statistical calculations.

Modified Mean (μ_y)	412.50	MPa
Deviation (σ_y)	12.21	MPa
Coef. of one-sided t.	2.755	
S_w	378.86	MPa

Figure 36 The final step of Staircase Method analysis

S_w represents the fatigue limit in accordance with the Staircase Method. The final fatigue limit was obtained by (3.1).

$$S_W = \mu_Y - t_{one-sided} * \sigma_Y \quad (3.1)$$

3.3.5. Kitagawa – Takahashi Analysis

Kitagawa – Takahashi diagrams were constructed in order to evaluate the relationship between fatigue life and defect size (Figure 42) [93]. This diagram gives a perspective for a detailed investigation of stresses with corresponding flaw sizes rather than conservative evaluation. Kitagawa – Takahashi diagram consists of two types of fatigue specimen: unnotched and notched. Unnotched fatigue tests were performed as previously mentioned in 3.3.4. Notched fatigue tests were conducted with specimens including artificial defects. Artificial defects were created by Vickers indenter and WEDM (wire-electro discharge machining) in various sizes. Artificially formed notches by indenter and WEDM are given in Figure 37.

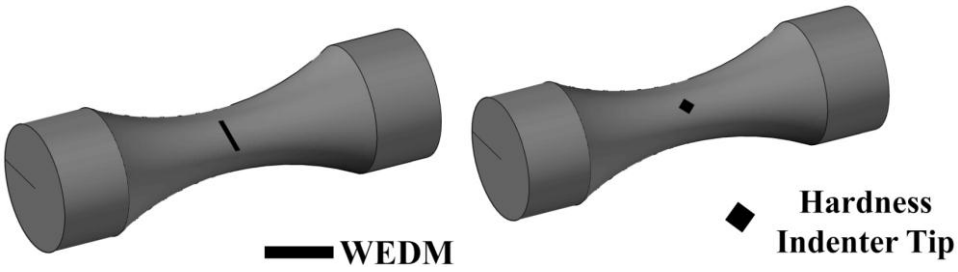

Figure 37 An illustrative drawing of notches created on fatigue specimens

WEDM machine with 0.25 mm wire spool size was used in this study. As the wire touches the specimen surface, a spark was induced by the discharge mechanism on the surface of the specimen which creates a defect that has a straight shape as illustrated in Figure 37. On the other hand, pyramidal shapes were created by Vickers hardness indenter tip. A portable specimen mold was printed with the 3-D printer at the beginning. The specimen was placed into the lower mold and hardness indenter was inserted through the upper mold as shown in Figure 38. It enabled the hardness indenter to create the notch as symmetrical as possible. Vickers hardness equipment was used with 30 kilogram-force (appx. 294 Newton) configuration.

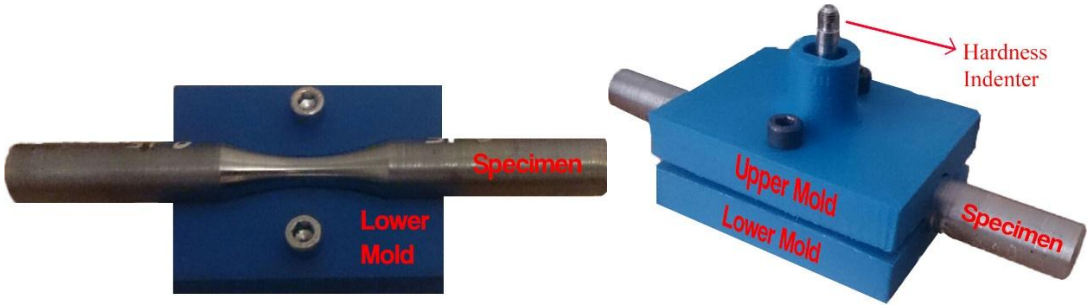

Figure 38 The equipment for creating notches on the specimen by hardness indenter

Kitagawa-Takashi diagram is one of the known approaches, however, this diagram itself gives a conservative approximation. Thus, El-Haddad introduced a new mathematical expression to determine the reduced fatigue limit and the detailed relationship between flaw size [46]. El-Haddad curve fit method draws a mathematical expression to represent Kitagawa diagram obtained by experimental methods. It

determines the critical size limit for critical cracks (a_0) and reduced fatigue limit ($\Delta\sigma$) which can be utilized in determination of threshold stress intensity factor for critical crack propagation ΔK_{th} [94, 95]. Since the reduced fatigue strength is directly related to fatigue strength and defect size, the relation can be given by (3.3).

$$\Delta S_w = \Delta S_{w0}\left(\frac{a_0}{a + a_0}\right) \tag{3.3}$$

where ΔS_w is the reduced fatigue strength, ΔS_{w0} is the fatigue strength of the material in unnotched condition, a is notch size, and a_0 is initial crack size. El-Haddad used a straight critical crack size (a_0) in this curve fitting equation [96]. However, flaws are formed in a semi-elliptical shape rather than straight in our case. Thus, flaws and defects were evaluated according to Murakami's $\sqrt{area}$ method [97]. This method was basically based on area measurement of inclusion, and artificially formed indenter tip and WEDM marks were measured with respect to it in this study. On the other hand, notch geometries were given in Figure 39.

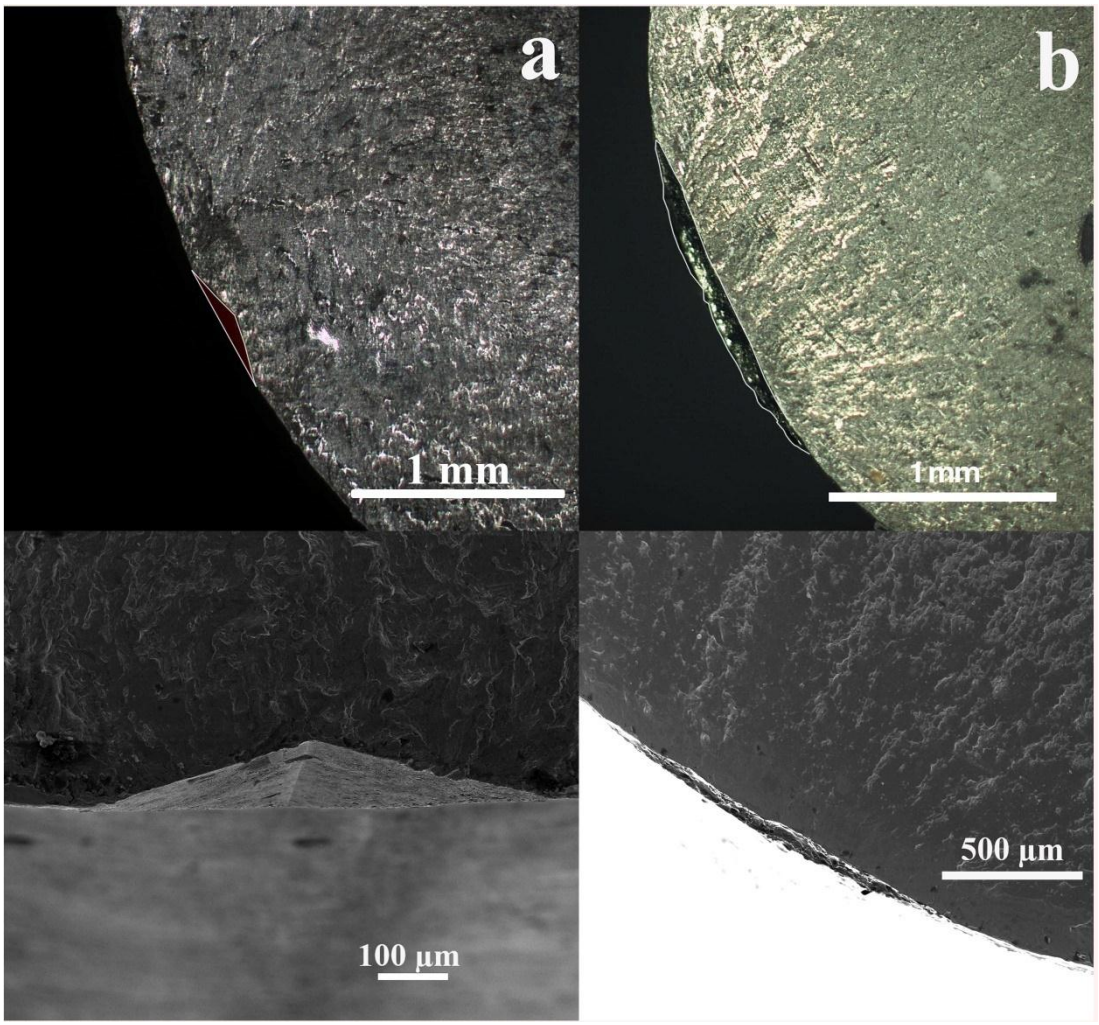

Figure 39 The SEM and optic micrographs of notches by a) hardness indenter tip, b) WEDM

Murakami suggested that the square root area of the created notch on the surface and perpendicular to the stress direction gives the most critical length (Figure 40). This assumption has no mathematical background; however, it was verified by experimental studies by Murakami [97].

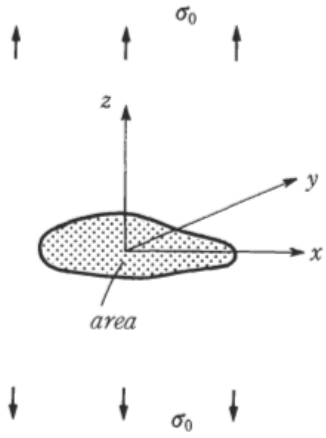

Figure 40 An illustrative drawing of a suitable defect geometry that is in accordance with Murakami square root area method [97]

On the other hand, it was concluded that the geometry factor of notches that are created on the surface is appx. 0.65 [20, 97]. This assumption is based on the stress intensity factor for an arbitrary shaped 3D surface crack model (Figure 41).

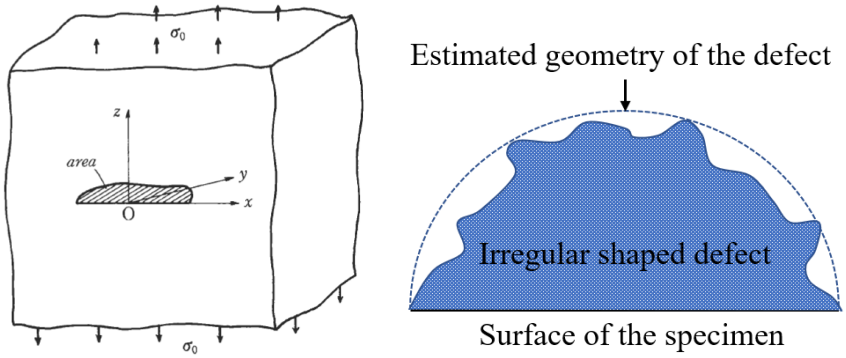

Figure 41 A representative drawing of irregularly shaped defects on the surface

An estimated approach for threshold intensity factor ($K_{I,max}$) for critical cracks is given by (3.4) [97].

$$K_{I,max} = 0.65\Delta S_w\sqrt{\pi\sqrt{area_0}} \qquad (3.4)$$

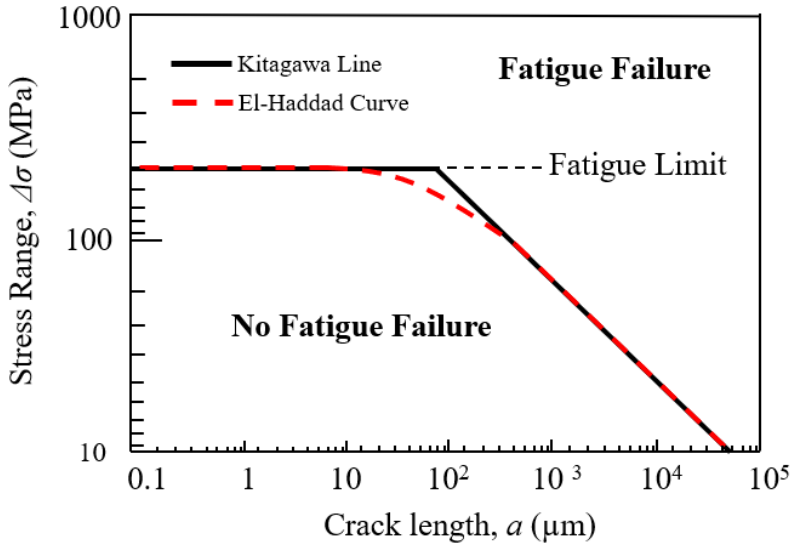

Figure 42 An illustrative Kitagawa – Takahashi diagram

3.4. Investigation of Fracture Surfaces of the Test Specimens

Fracture surfaces of fracture toughness test specimens were carefully examined and measured to determine a_0 in order to calculate CTOD and K values. Fatigue test specimens were prepared for optical microscope examination. Fracture surfaces of the broken fatigue test specimens were investigated by optical microscopy in order to determine the initial notch sizes that will be used in Kitagawa – Takahashi diagrams.

CHAPTER 4

RESULTS AND DISCUSSION

4.1. Chemical and Microstructural Characterization

AISI 4135 has good hardenability due to the presence of Mn and Mo [98], however, it is hard to obtain fully transformed structures at the end of the heat treatment or quenching in thick components in some cases. The results of the Jominy quenched-end test for AISI 4135 is given in Figure 43.

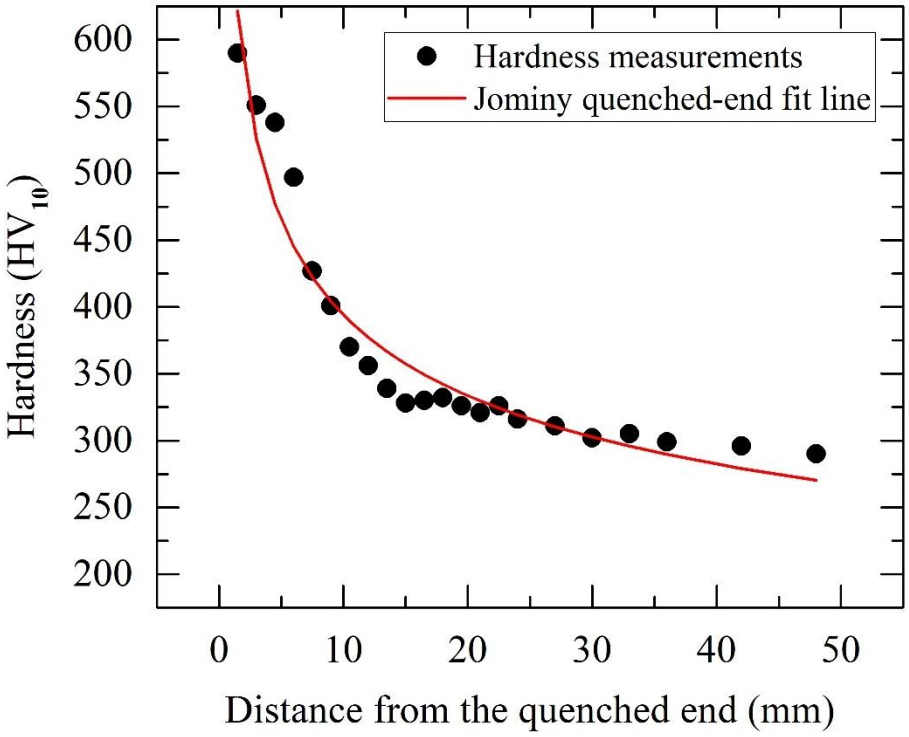

Figure 43 Hardenability of AISI 4135 material

Spectral analysis performed by Optical Emission Spectrometer showed a deviation compared to given technical specification, i.e., Manganese content was found to be lower, contrarily, phosphorus content higher as given in p. 30.

Manganese addition is preferred when high carbon diffusion rate is needed. If there is slightly less manganese content, it may cause hot cracking by forming FeS. As the MnS formation is increased, machinability of material is increased as well. Furthermore, reduction in sulfur content leads to less brittleness since sulfur is the main factor for brittleness. However, overaccumulation of manganese itself in steel may also result in brittleness [98-100]

Phosphorus is the main solid-strengthener second to carbon in ferrite structure. Phosphorus has beneficial effects regarding yield and tensile strength in case of small amount of adding such as up to 0.25% by weight. It enhances the capability of cold-working for steels, as well as, machinability and corrosion resistance [101, 102]. On the contrary, detrimental effects of phosphorus are unavoidable when the phosphorus content exceeds 0.25% by weight. Phosphorus causes loss of both ductility and toughness. An increase in phosphorus content can conduce to temper embrittlement in consequence of phosphorus segregation at austenite grain boundaries. Additionally, it leads to grain coarsening resulting in the undesired segregation [103].

Grain Size Measurements in accordance with the Intercept Procedure in the ASTM E112-13 [104] showed that the average grain size of the as-received material is 18.4 μm (ASTM No. 8.2).

4.1.1. Heat Treatments

Specimens were held at 870°C for 1 hour to obtain fully-austenitic microstructure. Then the specimens were quenched in oil to prevent quenching cracks. Next, various tempered martensite structures were obtained by tempering at several temperatures. The complete heat treatment mapping was done according to the Jmat Pro model.

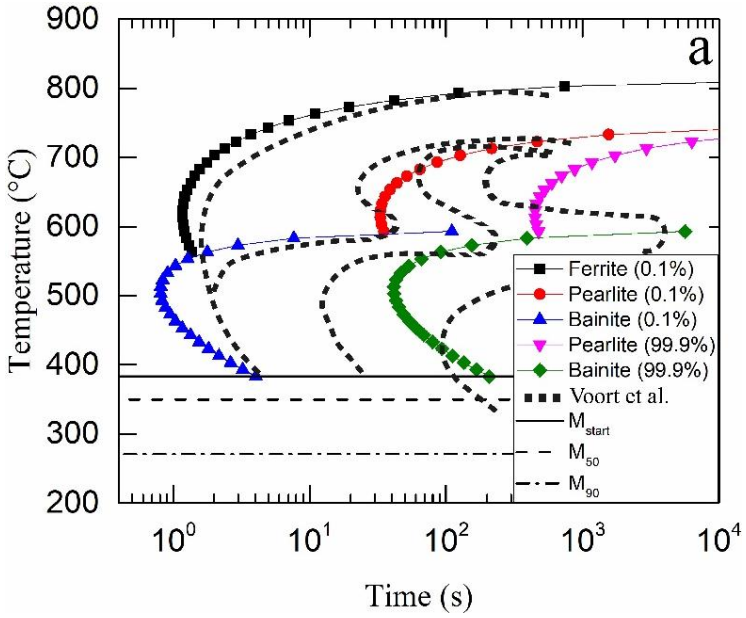

Figure 44 The comparison of Jmat Pro results and those obtained by Voort et al. [89]

Time for the formation of martensite calculated by the JMat Pro is shorter than that reported by Voort et al. [85]. The results are illustrated in Figure 44. The difference is caused by manganese content. Since the studied axle material has low manganese content, the cooling time for martensite formation decreases, therefore, critical cooling rate increases. Different type of microstructural formations was done according to transition temperatures (Table 4) obtained by heat treatment mapping.

Table 4 Transition temperatures of the phases for AISI 4135 steel

Microstructure	Transition Temperature (°C)
Ferrite	811
Pearlite	750
Bainite	593
Martensite	376

23 different heat treatments were performed, and 15 of them were selected as prospective configuration during the study (Table 5) to obtain tempered martensite and bainite.

Table 5 Heat treatments applied to the AISI 4135 specimens

Low Tempering Temperature	Mid Tempering Temperature	High Tempering Temperature	Bainite Formation	Bainite Formation with Water Quench
A1-180-QT4	A1-540-QT4	A1-700-QT4	A1-350-B1	A1-350-B1-WQT
			A1-350-B4	
A1-190-QT4	A1-540-QT7		A1-350-B7	
			A1-400-B1	A1-400-B1-WQT
A1-180-QT24	A1-540-QT24		A1-400-B4	
			A1-400-B7	

A is austenitization, QT is quenched in oil and tempered, B is bainite, WQT is water quenched and tempered, and the number given after A, T and B represent time in hour. Among fifteen different heat treatments, prospective materials were selected due to their morphological properties and hardness values which are indicated in Table 6.

Table 6 Studied microstructures with process details

Microstructure	Tempered Martensite (twinned) with carbides	Tempered Martensite with globular carbides	Lower Bainite	Ferrite – Pearlite (As-received)
Austenitization Temperature (°C) / Time (h)	870/1h	870/1h	870/1h	870/1h
Quenching in	Oil	Oil	-	-
Tempering Temperature (°C) / Time (h)	540/4h	700/4h	-	-
Bainite Formation Temperature (°C) / Time (h)	-	-	400/7h	-
Cooling	Air	Air	Air	Controlled Environment

Samples were categorized as comparison groups which are given in Table 7.

Table 7 Comparison groups of the samples

Group	Combination	Constant and Variable Parameters
1	Tempered Martensite (540°C/4h) + Tempered Martensite (700°C/4h)	Tempered Martensite Different Tempering Temperatures
2	Tempered Martensite (540°C/4h) + Lower Bainite (400°C/7h)	Similar Hardness Values Different Microstructures
3	Ferritic-Pearlitic	Current Axle Microstructure

Comparison groups were created to comparatively evaluate the microstructural and morphological properties. The ferritic-pearlitic structure was compared with the other microstructures for service feasibility, too.

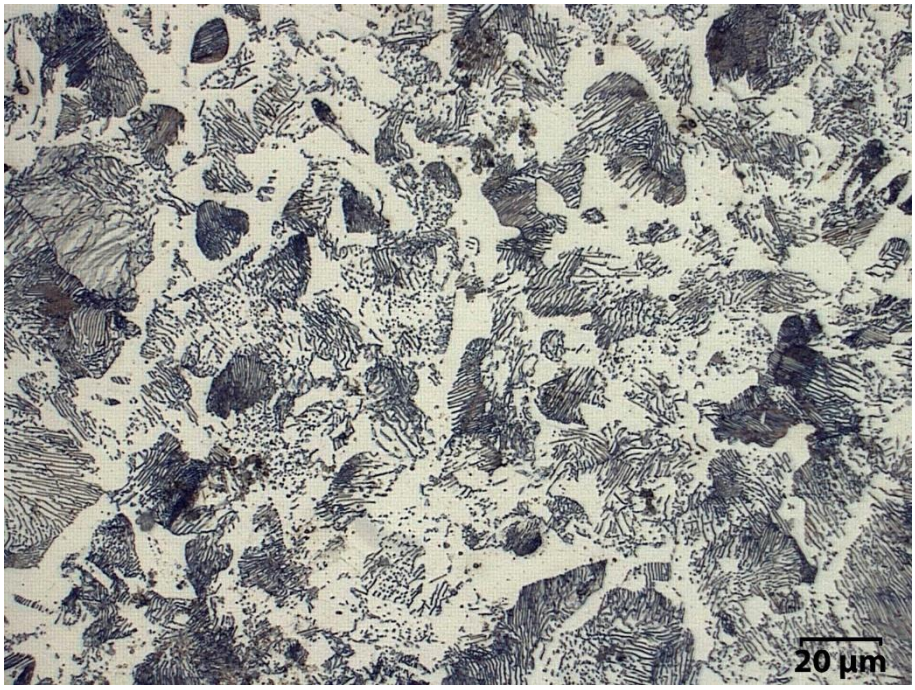

Figure 45 Optical micrograph of the ferritic-pearlitic structure

Figure 46 Optical micrograph of the tempered martensite (540°C/4h)

Figure 47 Optical micrograph of the tempered martensite (700°C/4h)

Figure 48 Optical micrograph of lower bainite (400°C/7h)

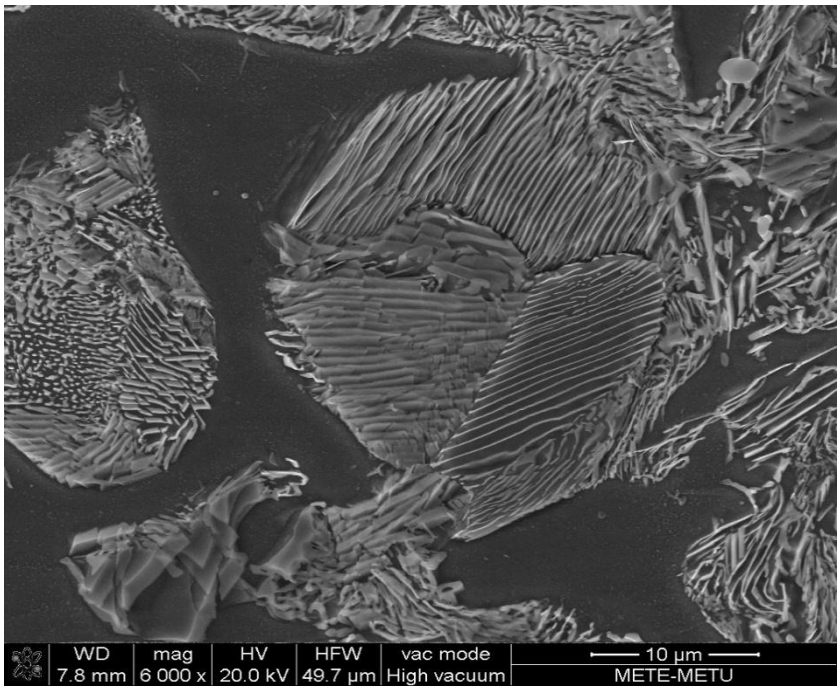

Figure 49 SEM micrograph of the ferritic-pearlitic structure

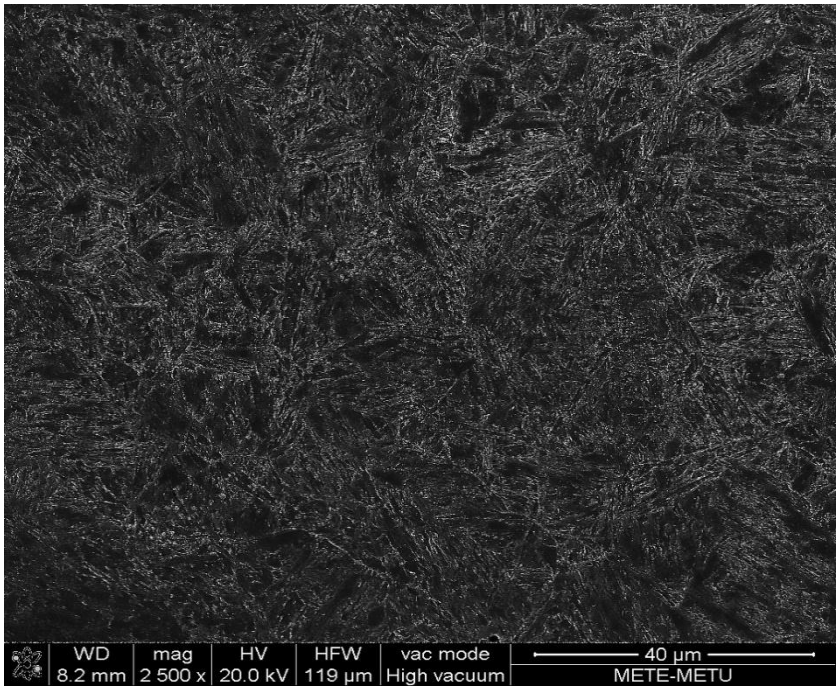

Figure 50 SEM micrograph of the tempered martensite (540°C/4h)

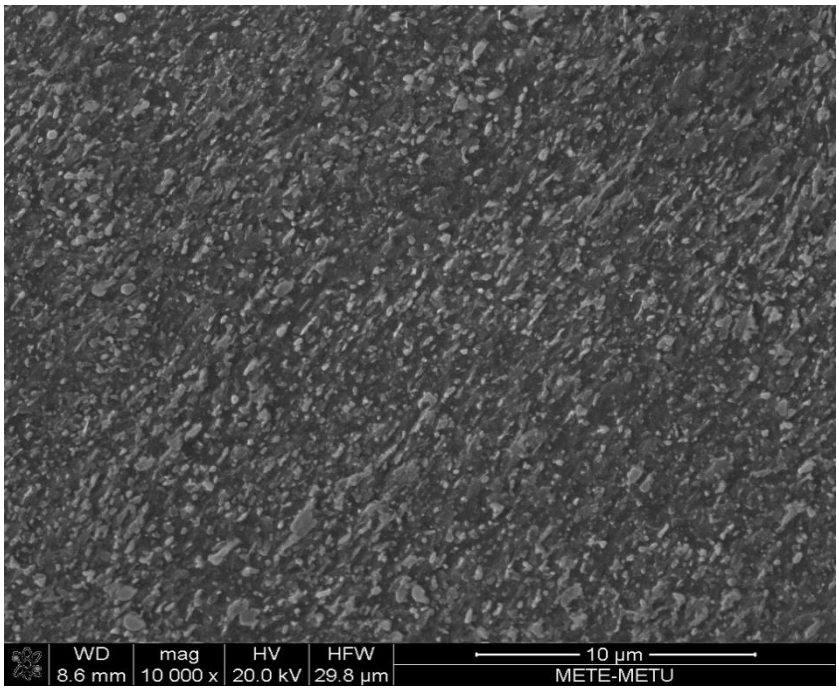

Figure 51 SEM micrograph of the tempered martensite (700°C/4h)

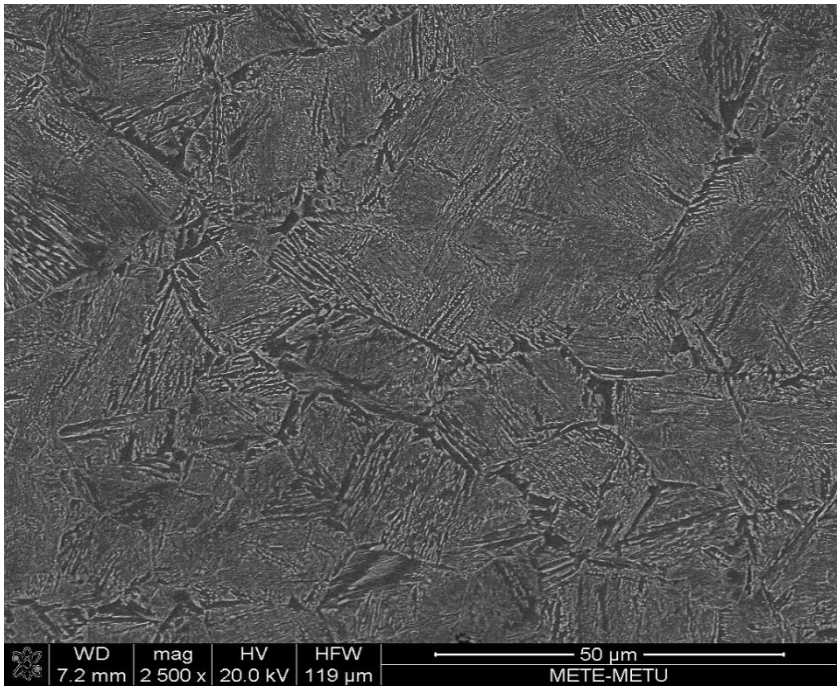

Figure 52 SEM micrograph of lower bainite (400°C/7h)

Optical and SEM micrographs of the as-forged (as-received) sample are given in Figure 45 and Figure 49. Since it was cooled in an environment-controlled furnace with a low cooling rate, it has a ferritic-pearlitic structure.

Optical and SEM micrographs of the sample tempered at 540°C for 4h are given in Figure 46 and Figure 50 respectively. The microstructure consists of carbides particles in a twinned martensitic structure since tempering temperature is neither high to form globular carbides nor low to obtain needle-like carbides. Therefore, it has not high-stress concentration compared to those tempered at lower temperatures.

Optical and SEM micrographs of the sample tempered at 700°C for 4h are given in Figure 47 and

Figure **51** respectively. Due to high tempering temperature, it has globular carbide particles caused by increased carbon precipitation rate.

Optical and SEM micrographs of the bainitic sample (isothermal holding at 400°C for 7h) are given in Figure 48 and

Figure **52** respectively. The microstructure consists of lower bainite. Since the formation time is high, there is some carbide precipitation that resembles upper bainite formation.

4.2. Mechanical Characterization

4.2.1. Tensile Test

The stress-strain curves are given in Figure 53. Tensile properties of the samples under monotonic stresses are presented in Table 8.

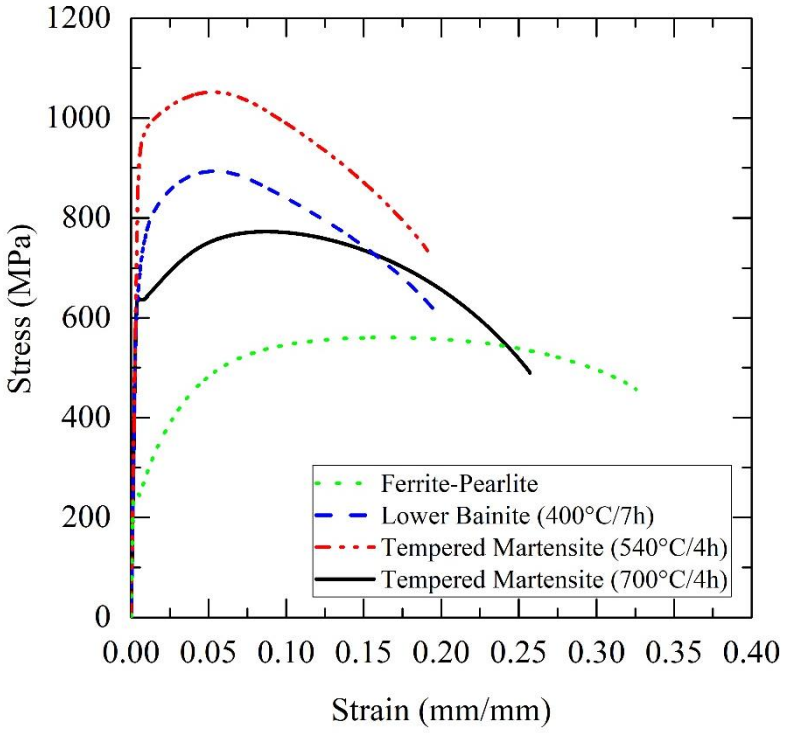

Figure 53 Overall axial stress-strain curves of the samples

Table 8 Tensile properties of samples under monotonic loading

Heat Treatments	E (GPa)	$R_{0.2}$ (MPa)	Rm (MPa)	EL (%)	Rm - $R_{0.2}$ Ratio	Strain Hardening Exponent, n
Ferrite-Pearlite	191	253	564	28	2.2	0.34
Tempered Martensite (700°C/4h)	201	638	773	26	1.2	0.33
Lower Bainite (400°C/7h)	197	683	893	20	1.3	0.41
Tempered Martensite (540°C/4h)	203	948	1052	15	1.1	0.44

The ferritic-pearlitic structure exhibited medium ductility due to ferrite structure since ductility is directly related to plastic deformation and grain size. As-received condition consists of ferrite bands and pearlite along the grain boundaries [105]. Since the ferrite-pearlite structure is dominant in as-received condition, yield and tensile strength are found to be lower compared to the others. However, if the cementite formation increases in as-ferritic-pearlitic condition, ductility conversely decreases. Furthermore, since the cooling rate is quite low regarding other conditions, ductility increases due to higher interlamellar spacing and bigger pearlite colonies.

The relationship between yield and tensile strength completely depends on elastic-plastic deformation capability, thus, microstructural configuration. An increase in plastically deformability thanks to the microstructural configuration can enhance the ratio between tensile and yield strength. Among samples, the highest plastic deformation was obtained by as-received condition material, concurrently yield – tensile strength ratio as 2.2. Furthermore, it shows that the ferritic-pearlitic condition has monotonic hardening behavior. Overall tensile – yield strength ratio is given in Table 8.

On the other hand, the highest yield and tensile strength were observed in tempered martensite (540°C/4h). Martensite volume fraction increases with increasing tempering temperature. On the contrary, the carbon percentage of martensite decreases with increasing volume fraction, which in turn, decrease in tensile and yield strength. It was also shown by Pouranvari [106] that the decrease in yield and tensile properties can be linked to carbon precipitation at higher tempering temperatures. On the other hand, reduction in martensite volume fraction leads to an increase in ductility, in other

words, plastic deformability. Therefore, the tensile – yield strength ratio is higher at tempered martensite (700°C/4h) rather than at tempered martensite (540°C/4h).

The bainitic structure also exhibits higher yield and tensile strength compared to ferritic-pearlitic microstructure (as-received condition) since bainite has finer grain distribution. Furthermore, Sawley [107] indicated that the improvement in tensile properties of bainite structure as a result of the vast amount of distributed dislocations.

4.2.2. Hardness Test

Hardness measurements were performed on dummy specimens and at the edge of the tensile and fatigue specimens to validate whether the applied heat treatments were accurate. Results of hardness measurement graph are given in Figure 54. Hardness results were obtained by the measurement on the longitudinal direction (Table 9).

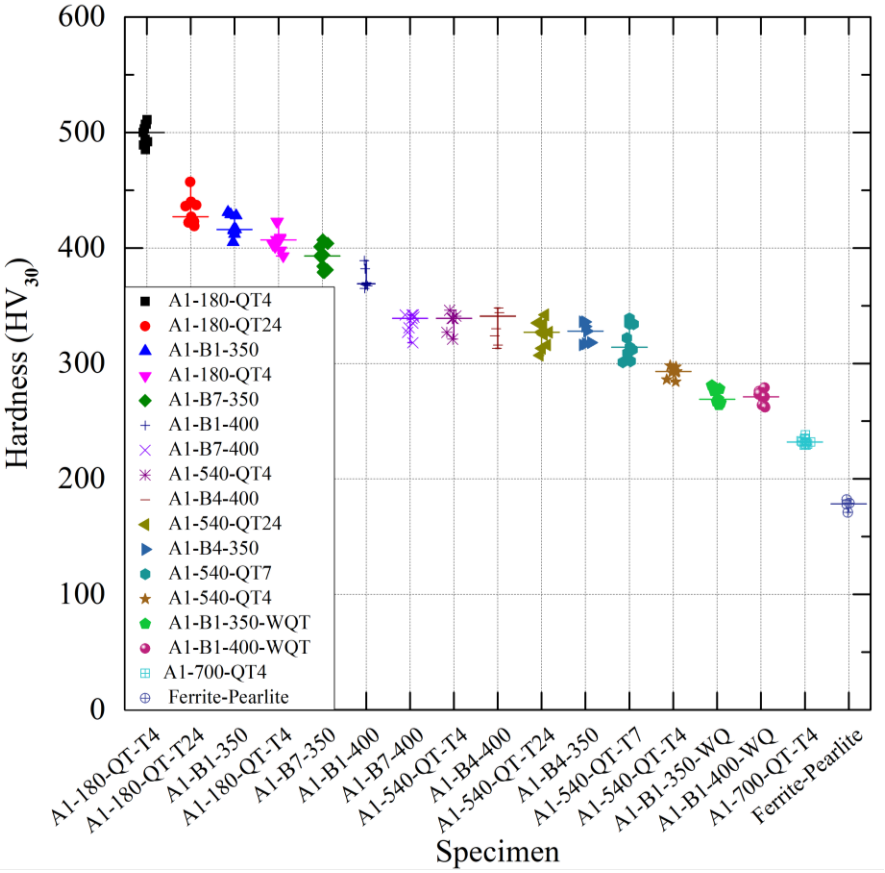

Figure 54 Overall hardness results in the longitudinal direction

A is *austenitization*, B is *bainite*, QT is *quenched in oil and tempered*, WQT is *quenched in water and tempered*, and the number given after A, T, and B represents time in hour.

Table 9 Longitudinal hardness measurements of the samples

Microstructure	Longitudinal (HV)		
	Min.	Max.	Avg.
Ferrite-Pearlite	171	182	177
Tempered Martensite (700°C/4h)	229	238	234
Lower Bainite (400°C/7h)	318	342	333
Tempered Martensite (540°C/4h)	321	346	334

As the carbon content in microstructure increases and tempering temperature decreases, the hardness of microstructure increases [25]. Carbides start to precipitate in the globular form instead of needle and plate-like form with the increasing tempering temperature. Thus, 540°C-tempered martensite has higher hardness value than 700°C-tempered martensite. On the other hand, the bainitic sample has higher hardness compared to ferritic-pearlitic sample since bainite is an interphase.

4.2.3. Fatigue Test

Fatigue test results of the samples are given in Figure 55 and the fatigue limit values are given in Table 10.

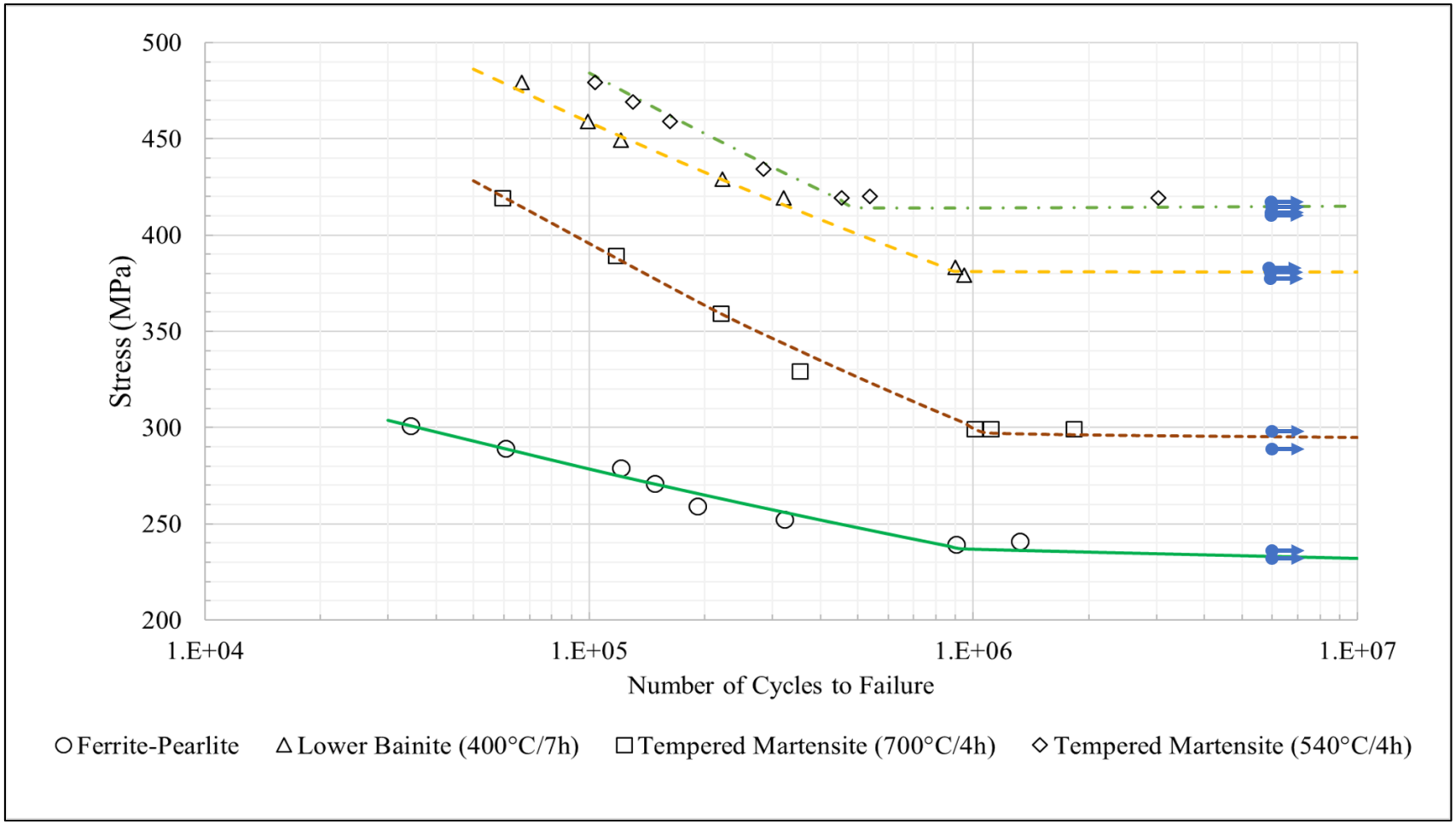

Figure 55 S-N curve of the samples

Table 10 Fatigue limits of the samples

Material	Fatigue Limit (MPa)	Lower Fatigue Limit ($C_{0.95}P_{0.90}$) (MPa)
Ferrite-Pearlite	230	211
Tempered Martensite (700°C/4h)	296	261
Lower Bainite (400°C/7h)	381	354
Tempered Martensite (540°C/4h)	416	381

C, *confidence level,* is the level of the included population, and P, the *probability of survival*, is the rate of having no fatigue failure. T values were chosen based on normal distribution. Degrees of freedom was found to be 18 and corresponding T value was 2.1009. The reduction was carried out by (4.1).

$$Sw_{Lower\ Bound} = Sw - \sigma t_{value} \tag{4.1}$$

where Sw is fatigue limit, σ is standard deviation, and t_{value} is a constant from Student's t Distribution Table.

The highest fatigue limit was obtained by tempered martensite (540°C/4h) among the other samples. The ferritic-pearlitic structure has the lowest fatigue limit others owing to saturation of carbon content is very low. Although this structure has high ductility, it still has unfavorable mechanical properties in terms of yield, tensile, fatigue and fracture toughness.

Martensite is very hard and brittle phase of steel; however, subsequent tempering enhances the toughness and ductility of martensitic structures. Furthermore, tempering relieves the residual stress which may cause distortion or cracking under service conditions. Yield, tensile, and fatigue strength decrease with the increasing tempering temperature. On the other hand, increasing tempering temperature enhances the toughness of the material [80].

Tempered martensite (540°C/4h) has highest fatigue strength since it has the lowest tempering temperature. Sorokin et al. indicated that the fatigue limit increases at lower temperatures, especially under 300°C, and then increasing tempering temperature

leads to a reduction in fatigue limit [108]. Moreover, the stable ferrite and pearlite content are lower since tempering temperature is relatively lower than tempered martensite (700°C/4h).

Bainite is obtained from austenite by moderate cooling. Bainite is an interphase between pearlite and martensite. Lower bainite was obtained by isothermal heating at 400°C for 7h. It includes cementite distributed along the structure and has higher fatigue limit compared to the sample tempered at 700°C.

There is a solid relationship between fatigue strength and the other mechanical properties. The higher yield strength causes the material to become more durable against cyclic loadings. On the other hand, hardness can be indirectly related to the fatigue strength. After ranking the hardness values for the highest to the lowest, it is seen that the hardness can extend the fatigue limit due to retardation in crack formation rather than crack propagation. Furthermore, crack propagation is directly related with fracture toughness of the material. As a result, the most advantageous microstructure is 540°C tempered martensite in terms of fatigue strength.

Modified S-N curves in terms of σ_a/σ_{wf} (stress amplitude/fatigue limit) and N_f (the number of cycles to failure) are given in Figure 56. These curves basically express the damage tolerance capability against fatigue failure. As the σ_a/σ_{wf} decreases, plastic deformation capability of the material decreases. It is clearly seen that for the $1.2 \times 10^6 - 1.3 \times 10^6$ cycle range, the safest microstructure against fatigue loading is the 700°C tempered one.

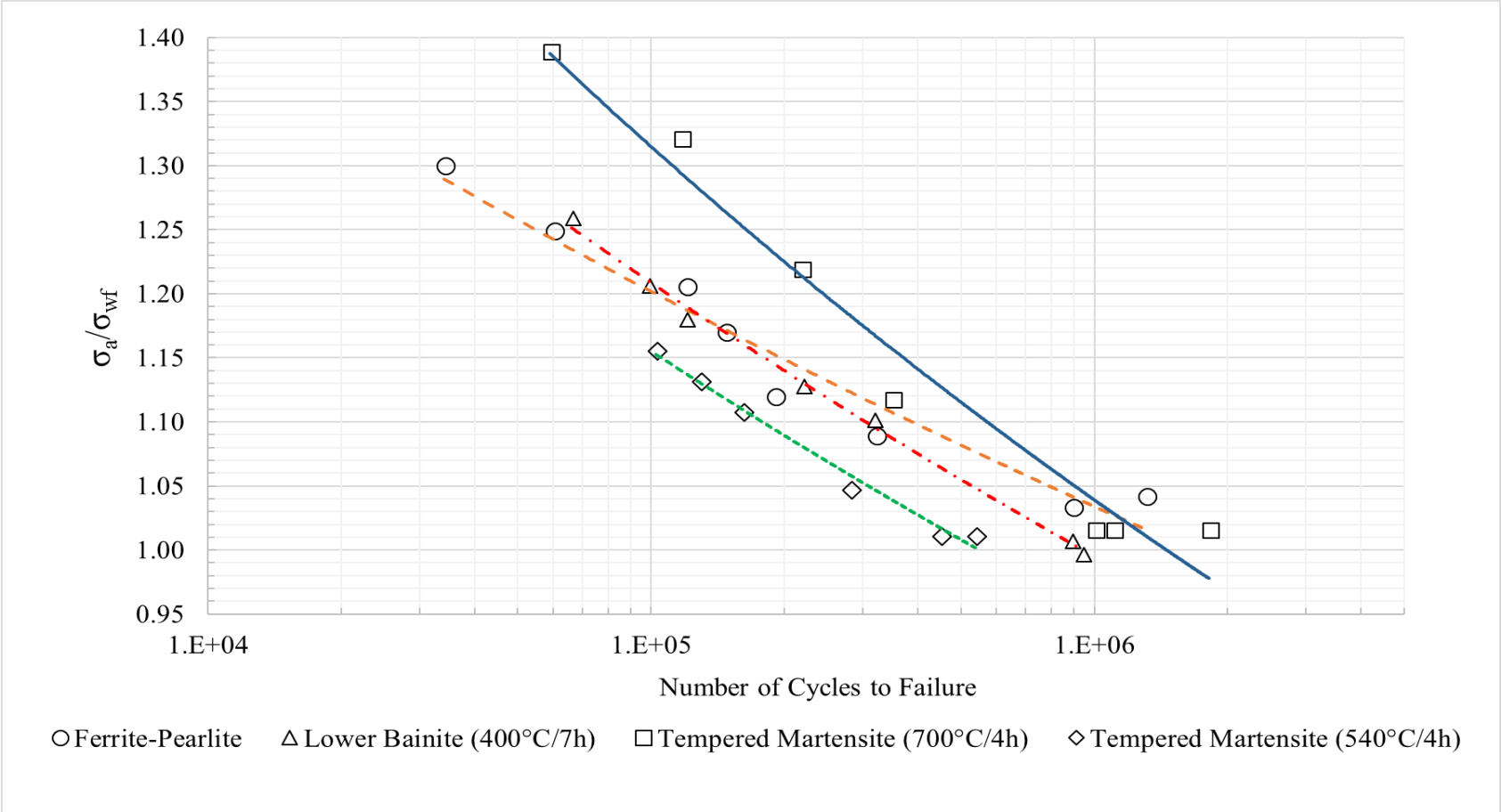

Figure 56 Modified S-N Curve

4.2.4. Fracture Toughness Test

The results are given in Table 11 and illustrated in Figure 57.

Table 11 Results of fracture toughness tests

Type of Microstructure	Max. Load (N)	CMOD (mm)	K_Q ($MPa.m^{1/2}$)
Lower Bainite (400°C/7h)	36706	0.42	105
Tempered Martensite (700°C/4h)	38514	3.70	96
Tempered Martensite (540°C/4h)	36434	0.37	94
Ferrite-Pearlite	29283	1.39	73

Ductility and fracture toughness of the lower bainite are higher than those of the tempered martensite for the equivalent hardness condition. However, lower bainite structure has lower yield strength since the size of bainite sheaves are relatively larger than the tempered martensite plates. It has been reported that bainite exhibits transgranular fracture behavior whereas tempered martensite exhibits intergranular fracture behavior [100]. Carbide precipitation along the grain boundaries in the tempered martensite is the main reason for intergranular fracture.

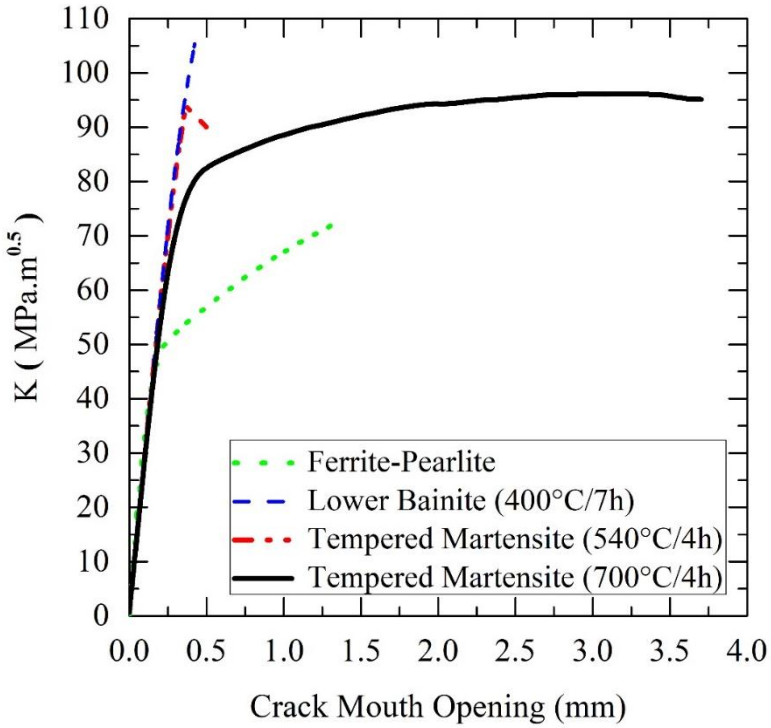

Figure 57 Fracture Toughness (K) versus Crack Mouth Opening (CMOD)

The highest fracture toughness value was obtained for the bainitic sample. Since lower bainite is brittle material, no plastic deformation was observed through the test. Furthermore, tempered martensite (540°C/4h) also exhibits linear-elastic behavior which has resulted in a brittle fracture. On the other hand, ferrite-pearlite and tempered martensite (700°C/4h) exhibited an elastic-plastic behavior where the material can be plastically deformed right after elastic fracture threshold limit. Fracture surfaces of the samples are shown in Figure 58.

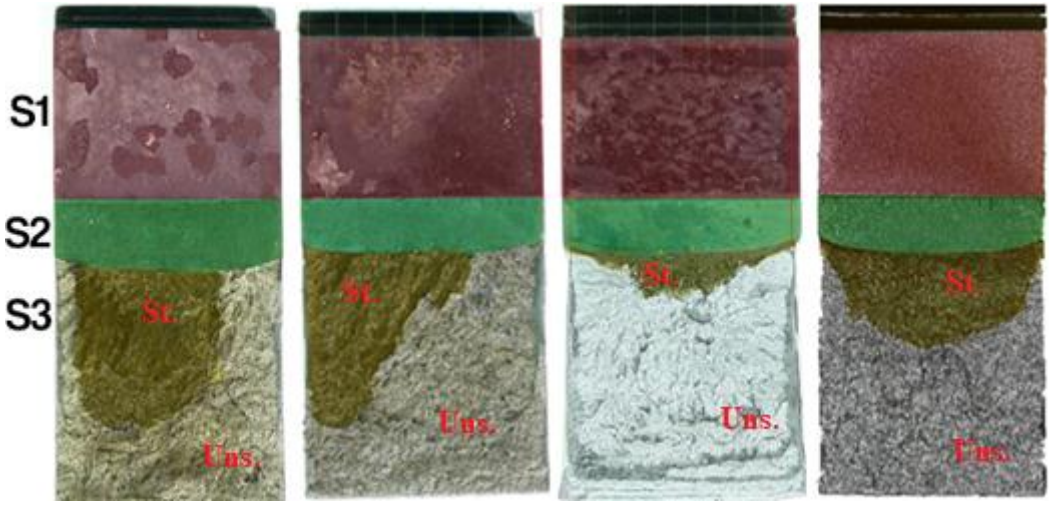

Figure 58 Fracture surface appearances of the samples having the microstructures of (a) lower bainite (400°C/7h), (b) tempered martensite (540°C/4h), (c) tempered martensite (700°C/4h), and (d) ferrite-pearlite

The red area, S1, is the first section that was machined by WEDM (wire-electric discharge machine). The green area, S2, represents the second section which was obtained by pre-cracking at R=0.1. The last and yellow area, S3, is the fracture area at the end of the fracture toughness test. The yellow areas exhibit the fracture behavior and the length of the fracture at the end of the test. The initial and the final length of the crack are input for the equation of fracture toughness. The yellow part of the samples (St.) represents the stable tearing. On the other hand, gray area (Uns.) represent unstable fracture at the end of the test.

4.2.5. Kitagawa – Takahashi Analysis

The Kitagawa diagrams are presented in Figure 59, Figure 60, Figure 61, and Figure 62. The overall results of four studied materials were given in Table 12. Area measurements of failed samples were done by OM and SEM analysis. The critical crack size estimation was done in according to Maximum Likelihood method (4.5). This unified approach consists of the approximation of an unknown parameter. In this study, critical crack length was assumed “the unknown parameter” and failed specimen

data was used as input for density function. The results were verified with the R^2 values since the most suitable critical crack length has the highest R^2 value.

$$L(\theta) = \prod_{i}^{n} f_x(x_i; \theta) \tag{4.5}$$

where $L(\theta)$ is likelihood function, f_x is density function, x_i number of data, and θ is the unknown parameter. The curve fitting technique consists of fitting of the broken samples with the lowest values. The fitting equation is generated from by estimating the best fitting by R2 value. If the fitting relatively covers the broken samples and R^2 value is high compared to other conditions, the estimated critical sizes can be found. Notch sizes were found to be 250-462 µm by WEDM, and 50-148 µm by hardness indenter tip.

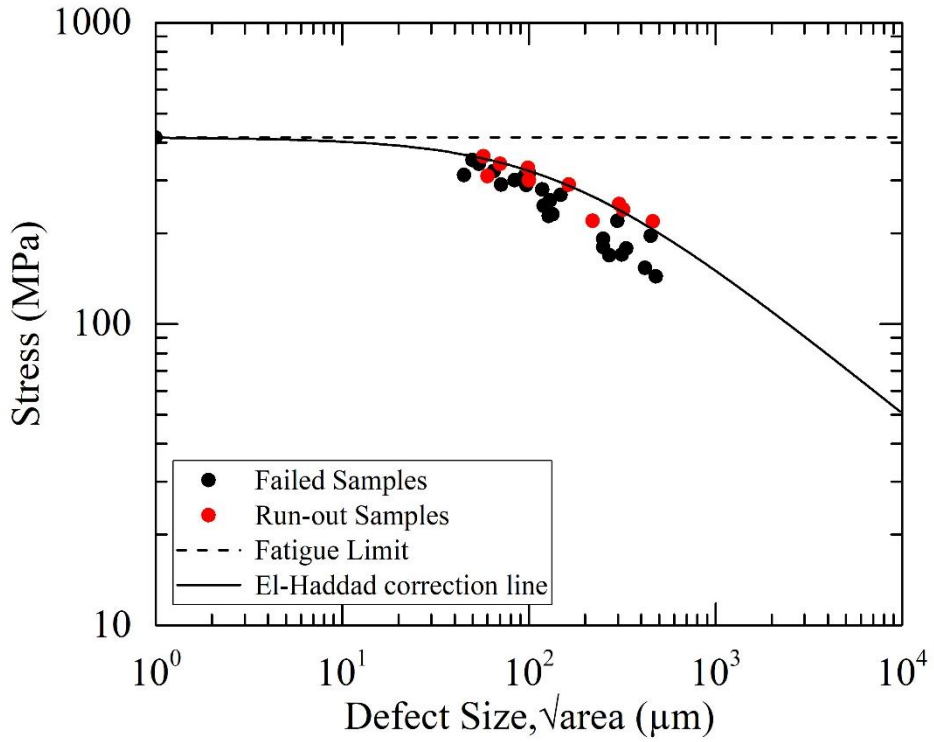

Figure 59 Kitagawa Analysis of the tempered martensite sample (540°C/4h)

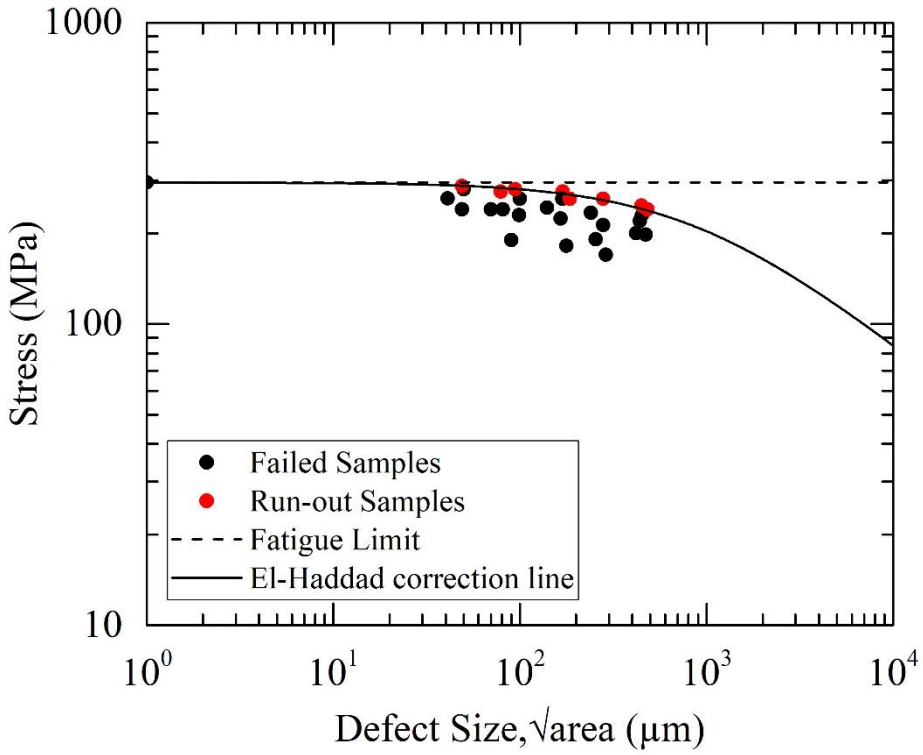

Figure 60 Kitagawa Analysis of the tempered martensite sample (700°C/4h)

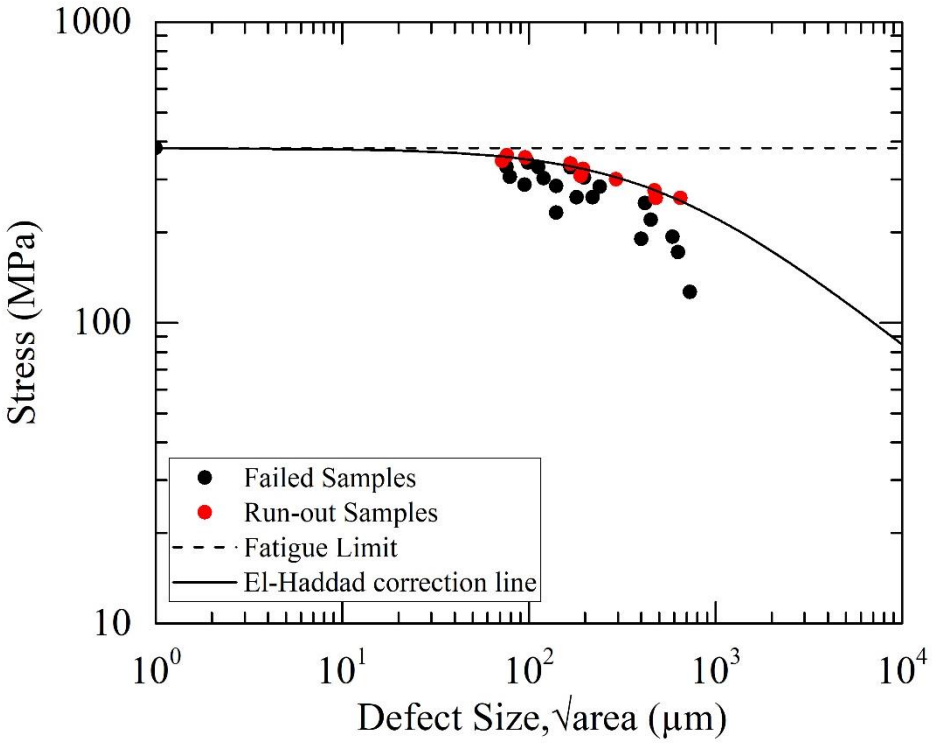

Figure 61 Kitagawa Analysis of the lower bainite sample (400°C/7h)

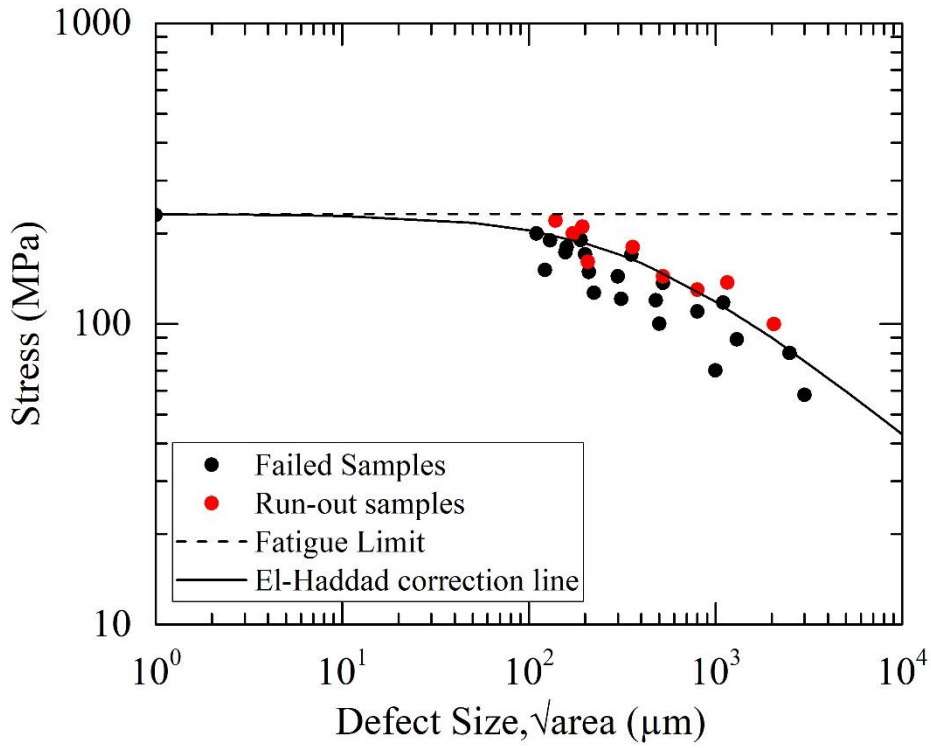

Figure 62 Kitagawa Analysis of the ferritic-pearlitic sample

Table 12 Summary of the Kitagawa Analysis results

Microstructure of the Samples	Fatigue Limit (MPa)	Critical Crack Limit, $area_0^{1/2}$ (μm)	Critical Stress Intensity Threshold, $K_{I,th}$ ($MPa.m^{1/2}$)
Tempered martensite (700°C/4h)	295	900	7.21
Lower Bainite (400°C/7h)	381	520	7.08
Tempered martensite (540°C/4h)	416	150	4.15
Ferrite-Pearlite	232	430	3.55

Fatigue strength plays a crucial role in the threshold intensity factor rather than $\sqrt{area}$ since fatigue strength can be modified by microstructural modification. Furthermore, material's elastic and plastic deformation capabilities can directly affect the critical crack propagation threshold of the material.

The tempered martensite sample at 540°C for 4h has the highest fatigue and the lowest critical crack limit among others. Although its toughness is high, it has high hardness, thus, cannot be plastically deformed. The fatigue crack behavior of this sample is quite

limited as shown in Figure 59. As soon as a notch with a size of 150 μm is formed, crack begins to propagate, hence, the long crack phenomenon occurs.

The tempered martensite sample at 700°C for 4h has the third highest fatigue limit and fracture toughness, conversely, its critical crack limit was obtained as $900\ \mu m$ (Figure 60). Since the tempering temperature is high, the microstructure contains globular carbide particles which the stress concentration is lower compared to other microstructural configurations. Its elongation value was determined as 26%, it can be concluded that it has a high deformability, hence, its fracture behavior was categorized under "elastic-plastic fracture mechanism". If an outer effect causes a notch on the surface of the material, the formed crack can be defined as "non-propagating critical crack" until 900 μm under service conditions.

It can be concluded that the highest critical crack thresholds were achieved for the 700°C-tempered martensite and bainitic samples. Even though the critical crack threshold of them are similar, 700°C-tempered martensite has a remarkable advantage in terms of the critical crack size limit.

The ferritic-pearlitic structure has the lowest fatigue limit, fracture toughness, and the critical crack threshold among others. Although it has a comparable critical crack size of 430 μm (Figure 62), it still has the lowest small flaw threshold 3.55 $MPa.m^{1/2}$, therefore, it only can be applicable for low-stress levels.

4.3. Fractographic Analysis of Microstructures

Fractographs of notched fatigue samples were given in Figure 63.The micrographs were taken from broken notched fatigue specimens and represents the stable cracking area of the fracture surface.

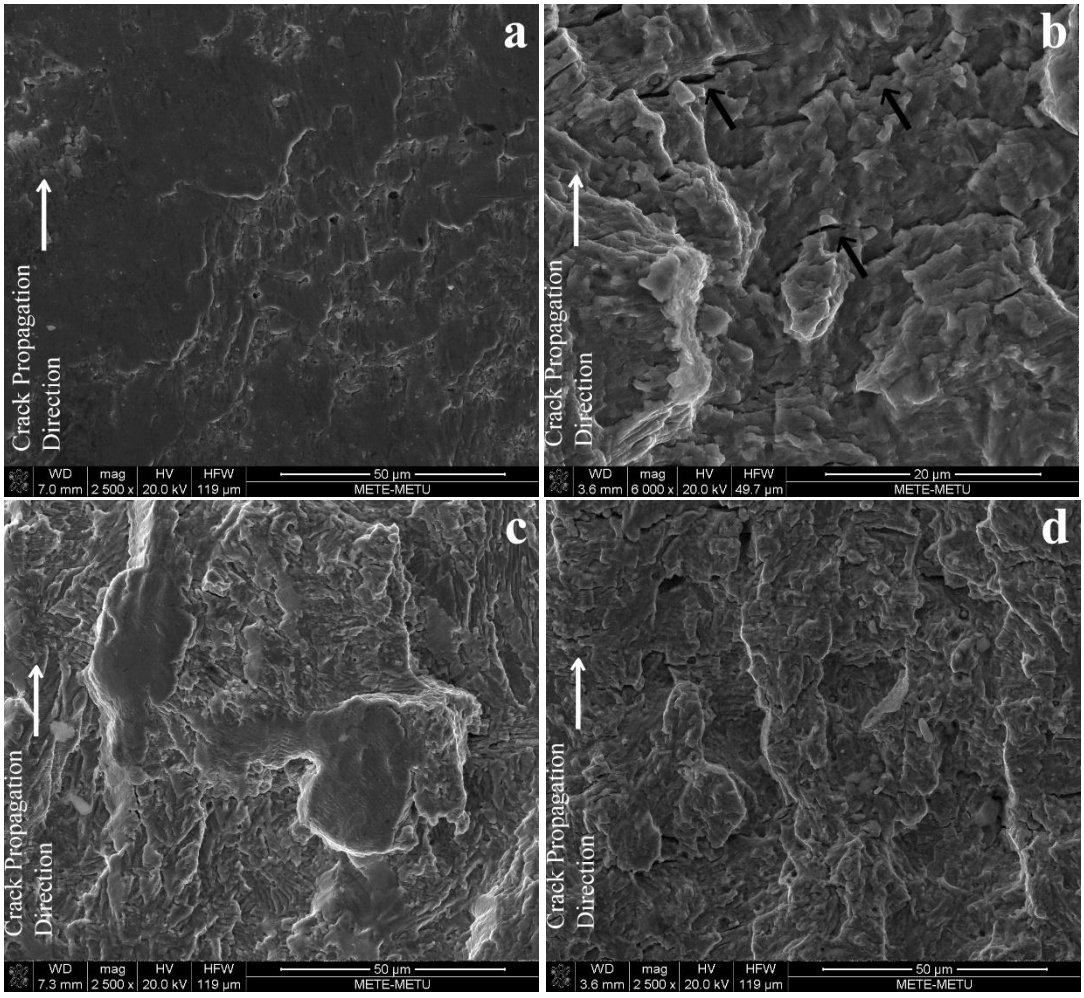

Figure 63 The fractographs of the samples a) ferrite-pearlite, b) 540°C-tempered martensite, c) lower bainite, and d) 700°C-tempered martensite

The ferritic-pearlitic structure shows no trace of fracture behavior. Since the ferritic-pearlitic structure is soft, rubbing effect is dominant in the fracture facet, and no secondary crack is observed (Figure 63.a). There are many secondary cracks observed (indicated by black arrows) in 540°C-tempered martensite (Figure 63.b). Since its plastic deformability behavior is poor, secondary crack formation instead of striations is quite inevitable. Lower bainite exhibit both brittle fracture crack propagation with some ductile tearing on the surface (Figure 63.c). There are some microcracking between phases, i.e., ferrite and bainite due to differences in their hardness. 700°C-tempered martensite shows local tearing, rubbing and striation since it has a medium-hard structure (Figure 63.d).

4.4. Overall Results

The overall results of mechanical and microstructural properties of samples were presented in Figure 64.

Microstructural Characterization

Martensite with twinned structure	Austenitized at 870°C for 1 hour Oil quenched and tempered at 540°C for 4 hours	
Martensite with globular cementite	Austenitized at 870°C for 1 hour Oil quenched and tempered at 540°C for 4 hours	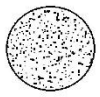
Lower bainite	Austenitized at 870°C for 1 hour Isothermal heating at 400°C for 7 hours	
Ferritic-Pearlitic	Austenitized above Ac3 Cooled in the temperature-controlled furnace	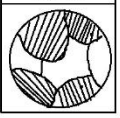

Mechanical Characterization

Hardness (HRC)

Microstructure	Min.	Max.	Avg.
Tempered at 540°C, 4h	**321**	**346**	**334**
Tempered at 700°C, 4h	229	238	234
Lower Bainite	**318**	**342**	**333**
Ferrite-Pearlite	171	182	177

Fatigue Strength (MPa)

Microstructure	Fatigue Limit (MPa)	SE (±)
Tempered at 540°C, 4h	**416**	**20**
Tempered at 700°C, 4h	296	41
Lower Bainite	381	31
Ferrite-Pearlite	232	18

Tensile Properties

Microstructure	E (GPa)	$R_{0.2}$ (MPa)	Rm (MPa)	EL (%)	Rm - $R_{0.2}$ Ratio	Strain Hardening Exponent, n
Tempered at 540°C, 4h	**203**	**948**	**1052**	15	1.1	**0.44**
Tempered at 700°C, 4h	201	638	773	26	1.2	0.33
Lower Bainite	197	683	893	20	1.3	0.41
Ferrite-Pearlite	191	253	564	**29**	**2.2**	0.34

Fracture Toughness

Microstructure	CMOD (mm)	$K_Q=K_{MAX}$ (MPa.$m^{1/2}$)
Tempered at 540°C, 4h	0.37	94
Tempered at 700°C, 4h	**3.70**	96
Lower Bainite	0.42	**105**
Ferrite-Pearlite	1.39	67

Kitagawa Analysis

Microstructure	Critical Crack Limit, $area_0^{1/2}$ (μm)	Critical Crack Threshold, $K_{I,th}$ (MPa.$m^{1/2}$)
Tempered at 540°C, 4h	150	4.15
Tempered at 700°C, 4h	**900**	**7.21**
Lower Bainite	520	7.08
Ferrite-Pearlite	430	3.55

Figure 64 The summary of the results

CHAPTER 5

SUMMARY AND CONCLUSION

The reduction in fatigue strength and corresponding crack sizes in microstructurally modified axle material were investigated by metallurgical and mechanical approaches. Fractographic features of fracture mechanism of microstructures were presented. The relationship between mechanical properties and critical crack threshold were examined throughout the study. It was concluded that the current microstructural configuration of AISI 4135 axles is inappropriate and modifications in the microstructure of the same steel by heat treatment will remarkably improve the service performance. The following conclusions can be drawn from this study:

- The AISI 4135 steel having ferritic-pearlitic microstructure is not feasible for axle applications since it exhibits the worst mechanical properties among the microstructural configurations investigated during the study. Microstructural modifications which result in either tempered martensite or lower bainite will improve the fatigue strength up to 44%, yield strength up to 60%, and tensile strength up to 27%. Additionally, the ductility of the 700°C-tempered martensite is two times higher than that of lower bainite and four times higher than that of 540°C-tempered martensite.
- The fracture toughness values of the lower bainite and 540°C-tempered martensite are two times larger than that of the ferrite-pearlite. It behaves in linear-elastic behavior manner as determined by elongation behavior.
- 700°C-tempered martensite has relatively poor fracture toughness in comparison to the lower bainite and 540°C-tempered martensite. However, it provides an advantage such that early crack detection is possible during two successive NDT inspections since it shows slow and stable tearing fracture behavior.

- There is no substantial relationship between fracture toughness and critical crack threshold.
- Kitagawa analysis was carried out to make an accurate assessment of the fluctuation of the fatigue strength concerning damage tolerance. The critical crack methodology was used as an approachment, and lower bainite and 700°C-tempered martensite were found to be the most applicable microstructure.
- The 540°C-tempered martensite gives the best static mechanical properties in terms of yield strength, hardness, and fatigue. However, this is not the case for the dynamic mechanical properties. For example, its allowable crack size limit is about five times lower than that of other microstructures at the fixed stress levels.
- Considering distortion and thermal stress, the bainitic microstructure seems to be the most appropriate choice for shafts and axles. However, obtaining fully-bainitic cross-section in the thick components is a challenging task. Similarly, quenching-tempering procedures are not feasible due to low hardenability of AISI 4135. Thus, focusing on microstructure modifications in the surface near zone might create new opportunities for improvement. For instance, if the presence of different microstructure layers along the thickness direction exists compressive residual stress states which positively affect the fatigue life.
- Globular carbides in the 700°C-tempered martensite seem to be advantageous for critical crack threshold since they reduce the stress concentration in the microstructure. However, in order to avoid the negative effect of overtempering on the damage tolerance, the size of the globular carbides should be optimized by careful tempering processes.

REFERENCES

1. Nishida, S.-I., *Failure Analysis in Engineering Applications*. 2014: Elsevier.
2. Yokobori, T., et al., *Proceedings of the First International Conference on Fracture: held in Sendai, Japan, September 12-17, 1965*. 1966: Japanese Society for Strength and Fracture of Materials.
3. Smith, R.A. and S. Hillmansen, *A brief historical overview of the fatigue of railway axles.* Proceedings of the Institution of Mechanical Engineers Part F-Journal of Rail and Rapid Transit, 2004. **218**(4): p. 267-277.
4. Norway, T.A.I.B., *Report on the air accident 8 September 1997 in the Norwegian sea approx. 100 NM west north west of Brønnøysund, involving Eurocopter AS 332L1 Super Puma, LN-OPG, operated by Helikopter Service AS*. 2001.
5. M., S., *Failure Analysis in Engineering Applications. Von Shin- ichi Nishida. Butterworth- Heinemann Ltd., Oxford 1992. Geb. £ 60.00*. Materials and Corrosion. Vol. 43. 1992. 584-584.
6. Carlson, A.S. and C.B. Gow, *Scrap Iron and Steel Industry.* Economic Geography, 1936. **12**(2): p. 175-184.
7. Rosenberg, N., *Inside the Black Box: Technology and Economics*. 1982: Cambridge University Press.
8. Zerbst, U., B. Madler, and H. Hintze, *Fracture mechanics in railway applications - an overview.* Engineering Fracture Mechanics, 2005. **72(**2): p. 163-194.
9. Smith, R.A., *The Versailles Railway Accident of 1842 and the First Research Into Metal Fatigue.(Retroactive Coverage).* Fatigue 90, 1990: p. 2033-2041.
10. Glynn, J. *On the causes of fracture of the axles of railway carriages*. in *Minutes of the Proceedings of the Institution of Civil Engineers*. 1844. Thomas Telford-ICE Virtual Library.
11. Stretton, C.E., *Safe Railway Working*. 1893: Crosby Lockwood and Son.
12. Suresh, S., *Fatigue of Materials*. 1998: Cambridge University Press.

13. Sendeckyj, G.P., *Constant life diagrams - a historical review*. International Journal of Fatigue, 2001. **23**(4): p. 347-353.

14. Broek, D., *Elementary Engineering Fracture Mechanics.* 1982.

15. Kumar, P., *Elements of Fracture Mechanics*. 2009: Tata McGraw-Hill Education.

16. Maršálek, P. and V. Moravec, *A methodology for gear fatigue tests and their evaluation (Part I).* Journal of Middle European Construction and Design of Cars, 2011. **9**(3): p. 13-17.

17. Krautkrämer, J., *Ultrasonic Testing of Materials*. 2013: Springer Science & Business Media.

18. Carboni, M. and S. Beretta, *Effect of probability of detection upon the definition of inspection intervals for railway axles.* Proceedings of the Institution of Mechanical Engineers Part F-Journal of Rail and Rapid Transit, 2007. **221**(3): p. 409-417.

19. Hirakawa, K., K. Toyama, and M. Kubota, *The analysis and prevention of failure in railway axles.* International Journal of Fatigue, 1998. **20**(2): p. 135-144.

20. Cantini, S. and S. Beretta, *Structural Reliability Assessment of Railway Axles*. 2011: Lucchini RS.

21. Marquis, G. and J. Solin, *Fatigue Design and Reliability*. Vol. 23. 1999: Elsevier.

22. Hirakawa, K. and M. Kubota, *On the fatigue design method for high-speed railway axles.* Proceedings of the Institution of Mechanical Engineers Part F-Journal of Rail and Rapid Transit, 2001. **215**(2): p. 73-82.

23. Makino, T., M. Yamamoto, and K. Hirakawa, *Fracture mechanics approach to the fretting fatigue strength of axle assemblies*, in *Fretting fatigue: current technology and practices*. 2000, ASTM International.

24. Totten, G.E., *Steel Heat Treatment: Metallurgy and Technologies*. 2006: CRC Press.

25. Callister, W.D. and D.G. Rethwisch, *Materials Science and Engineering*. Vol. 5. 2011: John Wiley & Sons NY.

26. Grum, J., *A review of the influence of grinding conditions on resulting residual stresses after induction surface hardening and grinding.* Journal of Materials Processing Technology, 2001. **114**(3): p. 212-226.

27. Sirin, S.Y., K. Sirin, and E. Kaluc, *Effect of the ion nitriding surface hardening process on fatigue behavior of AISI 4340 steel.* Materials Characterization, 2008. **59**(4): p. 351-358.

28. Waniuk, T.A., J. Schroers, and W.L. Johnson, *Critical cooling rate and thermal stability of Zr-Ti-Cu-Ni-Be alloys.* Applied Physics Letters, 2001. **78**(9): p. 1213-1215.

29. Nakamura, M., et al. *Effect of Alloying Elements and Shot Peening on Fatigue Strength of Carburized Steel*. in *International Conference on Shot Peening-4, Tokyo, Japan*. 1990.

30. Fu, Y., et al., *Improvement in fretting wear and fatigue resistance of Ti–6Al–4V by application of several surface treatments and coatings.* Surface and Coatings Technology, 1998. **106**(2): p. 193-197.

31. Ren, W.J., et al., *Evaluation of coatings on Ti-6Al-4V substrate under fretting fatigue.* Surface & Coatings Technology, 2005. **192**(2-3): p. 177-188.

32. Delosrios, E., et al., *Fatigue crack initiation and propagation on shot-peened surfaces in A316 stainless steel.* International Journal of Fatigue, 1995. **17**(7): p. 493-499.

33. Beretta, S., et al., *Corrosion–fatigue of A1N railway axle steel exposed to rainwater.* International Journal of Fatigue, 2010. **32**(6): p. 952-961.

34. Beretta, S., A. Ghidini, and F. Lombardo, *Fracture mechanics and scale effects in the fatigue of railway axles.* Engineering Fracture Mechanics, 2005. **72**(2): p. 195-208.

35. Wu, S.C., et al., *On the fatigue performance and residual life of intercity railway axles with inside axle boxes.* Engineering Fracture Mechanics, 2018. **197**: p. 176-191.

36. Domínguez Almaraz, G.M., J.L. Ávila Ambriz, and E. Cadenas Calderón, *Fatigue endurance and crack propagation under rotating bending fatigue tests on*

aluminum alloy AISI 6063-T5 with controlled corrosion attack. Engineering Fracture Mechanics, 2012. **93**: p. 119-131.

37. Hertzberg, R.W., *Deformation and Fracture Mechanics of Engineering Materials*. 1996: Wiley.

38. Stephens, R.I., et al., *Metal Fatigue in Engineering*. 2000: John Wiley & Sons.

39. Collins, J.A., *Failure of Materials in Mechanical Design: Analysis, Prediction, Prevention*. 1993: John Wiley & Sons.

40. Evans, P.R.V., N.M. Madhava, and T.G. Chart, *A fractographic study of fatigue failure in two high strength steels.* Czechoslovak Journal of Physics, 1969. **19**(3): p. 381-394.

41. Forsyth, P.J., *The Physical Basis of Metal Fatigue*. 1969: Blackie and Son LTD., London.

42. Jacoby, G., *Fractographic Methods in Fatigue Eesearch.* Experimental Mechanics, 1965. **5**(3): p. 65-82.

43. Dowling, N.E., *Mechanical Behavior of Materials: Engineering Methods for Deformation, Fracture, and Fatigue*. 2012: Pearson.

44. Makino, T., M. Yamamoto, and K. Hirakawa, *Fracture Mechanics Approach to the Fretting Fatigue Strength of Axle Assemblies,* in *Fracture Mechanics Approach to the Fretting Fatigue Strength of Axle Assemblies*. 2000.

45. Ruckert, C.O.E.T., et al., *On the relation between micro- and macroscopic fatigue crack growth rates in aluminum alloy AMS 7475-T7351*. International Journal of Fracture, 2006. **142**(3-4): p. 233-240.

46. Gürer, G. and C.H. Gür, *Failure analysis of fretting fatigue initiation and growth on railway axle press-fits.* Engineering Failure Analysis, 2018. **84**: p. 151-166.

47. Mughrabi, H., *On 'multi-stage' fatigue life diagrams and the relevant life-controlling mechanisms in ultrahigh-cycle fatigue.* Fatigue & Fracture of Engineering Materials & Structures, 2002. **25**(8-9): p. 755-764.

48. Beer, P. and E. Russel, *Mechanics of Materials.* McGraw-Hill International Edition, 1992.

49. Dieter, G.E. and D.J. Bacon, *Mechanical Metallurgy*. Vol. 3. 1986: McGraw-Hill New York.

50. Farahmand, B., *Elastic-Plastic Fracture Mechanics (EPFM) and Applications*, in *Fracture Mechanics of Metals, Composites, Welds, and Bolted Joints*. 2001, Springer. p. 180-236.

51. Materia, T. *Fracture Mechanics*. 2001; Available from: http://www.totalmateria.com/articles/Art45.htm.

52. Kanninen, M.F. and C.L. Popelar, *Advanced Fracture Mechanics.* 1985.

53. Taylor, D. and J.F. Knott, *Fatigue Crack-Propagation Behavior of Short Cracks - the Effect of Microstructure.* Fatigue of Engineering Materials and Structures, 1981. **4**(2): p. 147-155.

54. Ma, L. and A.M. Korsunsky. *Vector J-integral analysis of crack initiation at the edge of complete sliding contact*. in *Proceedings of the Royal Society of London A: Mathematical, Physical and Engineering Sciences*. 2006. The Royal Society.

55. Moore, P. and J. Nicholas. *The effect of inclusions on the fracture toughness of local brittle zones in the HAZ of girth welded line pipe*. in *ASME 2013 32nd International Conference on Ocean, Offshore and Arctic Engineering*. 2013. American Society of Mechanical Engineers.

56. Mach, K.J., D.V. Nelson, and M.W. Denny, *Techniques for predicting the lifetimes of wave-swept macroalgae: a primer on fracture mechanics and crack growth.* J Exp Biol, 2007. **210**(Pt 13): p. 2213-30.

57. Griffith, A.A., *The Phenomena of Rupture and Flow in Solids.* Phil. Trans. R. Soc. Lond. A, 1921. **221**(582-593): p. 163-198.

58. Irwin, G.R., *Analysis of stresses and strains near the end of a crack traversing a plate.* Journal of Applied Mechanics, 1957.

59. Delosrios, E.R., Z. Tang, and K.J. Miller, *Short crack fatigue behavior in a medium carbon steel.* Fatigue & Fracture of Engineering Materials & Structures, 1984. **7**(2): p. 97-108.

60. Suresh, S.O. and R.O. Ritchie, *Propagation of short fatigue cracks.* International Metals Reviews, 1984. **29**(1): p. 445-475.

61. Santus, C. and D. Taylor, *Physically short crack propagation in metals during high cycle fatigue.* International Journal of Fatigue, 2009. **31**(8-9): p. 1356-1365.

62. Pearson, S., *Initiation of fatigue cracks in commercial aluminium alloys and the subsequent propagation of very short cracks.* Engineering Fracture Mechanics, 1975. **7**(2): p. 235-247.

63. Neuber, H., *Theory of Notch Stresses: Principles for Exact Stress Calculation*. Vol. 74. 1946: JW Edwards.

64. Lawrence, F.V., *Mechanisms of Fatigue Crack Initiation and Growth*. 1994. 34.

65. Paris, P.C. and F. Erdogan. *A critical analysis of crack propagation laws*. 1963. ASME.

66. Sankaran, S., et al., *High cycle fatigue behaviour of a multiphase microalloyed medium carbon steel: a comparison between ferrite-pearlite and tempered martensite microstructures.* Materials Science and Engineering a-Structural Materials Properties Microstructure and Processing, 2003. **362**(1-2): p. 249-256.

67. Guan, M.F. and H. Yu, *Fatigue crack growth behaviors in hot-rolled low carbon steels: A comparison between ferrite-pearlite and ferrite-bainite microstructures.* Materials Science and Engineering a-Structural Materials Properties Microstructure and Processing, 2013. **559**: p. 875-881.

68. Laird, C., *The influence of metallurgical structure on the mechanisms of fatigue crack propagation*, in *Fatigue crack propagation*. 1967, ASTM International.

69. Wells, A.A. *Unstable crack propagation in metals: Cleavage and Fast Fracture*. in *Proceedings of the Crack Propagation Smposium*. 1961.

70. Rice, J.R., *A path independent integral and the approximate analysis of strain concentration by notches and cracks.* Journal of Applied Mechanics, 1968. **35**(2): p. 379-386.

71. El-Haddad, M.H., et al., *J integral applications for short fatigue cracks at notches.* International Journal of Fracture, 1980. **16**(1): p. 15-30.

72. Larsson, L.H., *Use of EPFM in Design*. Advances in Elasto-Plastic Fracture Mechanics. 1980. 261-278.

73. Cotterell, B., *Fracture and Life*. 2010: World Scientific.

74. Moore, P. and H. Pisarski, *CTOD and pipelines: the past, present, and future.* Journal of Pipeline Engineering, 2013. **12**(3).

75. Hashemi, S., et al. *Development of a laboratory test technique for direct estimate of crack tip opening angle*. in *ECF15, Stockolm 2004*. 2004.

76. Dugdale, D.S., *Yielding of Steel Sheets Containing Slits.* Journal of the Mechanics and Physics of Solids, 1960. **8**(2): p. 100-104.

77. Hutchinson, J.W., *Plastic Stress and Strain Fields at a Crack Tip.* Journal of the Mechanics and Physics of Solids, 1968. **16**(5): p. 337-+.

78. TSE, *EN 10083 Steels for quenching and tempering - Part 3: Technical delivery conditions for alloy steels*. 2006.

79. *ASTM A29 / A29M - 16 Standard Specification for General Requirements for Steel Bars, Carbon and Alloy, Hot-Wrought*. 2016.

80. ASTM, *ASTM E3-11 - Standard Guide for Preparation of Metallographic Specimens*. 2017.

81. ASTM, *ASTM A255-10 - Standard Test Methods for Determining Hardenability of SteeL*. 2014.

82. ASTM, *ASTM E18-17e1 - Standard Test Methods for Rockwell Hardness of Metallic Materials*. 2017.

83. Krauss, G., *Steels: Heat Treatment and Processing Principles.* ASM International, 1990, 1990: p. 497.

84. Totten, G.E. and M.A. Howes, *Steel Heat Treatment Handbook*. 1997: CRC Press.

85. Voort, V. and F. George, *Atlas of Time-Temperature Diagrams for Irons and Steels*. 1991: ASM international.

86. ASTM, *ASTM E8 / E8M-16a - Standard Test Methods for Tension Testing of Metallic Materials*.

87. ISO, *ISO 6892-1 - Metallic materials — Tensile testing — Part 1: Method of test at room temperature*. 2016.

88. ISO, *ISO 12107 - Metallic materials — Fatigue testing — Statistical planning and analysis of data.* 2003(E).

89. ISO, *ISO 1143 - Metallic materials — Rotating bar bending fatigue testing.* 2010.

90. ISO, *ISO 12135 - Metallic materials — Unified method of test for the determination of quasistatic fracture toughness.* 2016.

91. ASTM, *ASTM E399-12 - Standard Test Method for Linear-Elastic Plane-Strain Fracture Toughness K1C of Metallic Materials.* 2013.

92. ISO, *ISO 1099 - Metallic materials — Fatigue testing — Axial force-controlled method.* 2006.

93. Correria, J.A., et al., *A procedure to obtain the probabilistic Kitagawa-Takahashi diagram.* UPB Scientific Bulletin, Series D: Mechanical Engineering, 2016.

94. El Haddad, M.H., T.H. Topper, and K.N. Smith, *Prediction of non propagating cracks.* Engineering Fracture Mechanics, 1979. **11**(3): p. 573-584.

95. El Haddad, M., K. Smith, and T. Topper, *Fatigue crack propagation of short cracks.* Journal of Engineering Materials and Technology, 1979. **101**(1): p. 42-46.

96. El-Haddad, M.H., T.H. Topper, and K.N. Smith, *Prediction of non propagating cracks.* Engineering Fracture Mechanics, 1979. **11**(3): p. 573-584.

97. Murakami, Y., *Metal Fatigue: Effects of Small Defects and Non-metallic Inclusions*. 2002: Elsevier.

98. Crafts, W. and J. Lamont, *Effect of some elements on hardenability.* Trans. AIME, 1944. **154**: p. 386.

99. Nicholson, A. and J. Murray, *Surface hot shortness in low carbon steel.* J Iron Steel Inst, 1965. **203**(10): p. 1007-1018.

100. Tu, M.Y., et al., *Comparison of microstructure and mechanical behavior of lower bainite and tempered martensite in JIS SK5 steel.* Materials Chemistry and Physics, 2008. **107**(2-3): p. 418-425.

101. Craig, B.D., *The effect of phosphorus content on the hydrogen stress cracking of high strength 4130 steel.* Metallurgical Transactions A, 1982. **13**(5): p. 907-912.

102. Chen, H., H. Era, and M. Shimizu, *Effect of phosphorus on the formation of retained austenite and mechanical properties in Si-containing low-carbon steel sheet.* Metallurgical Transactions A, 1989. **20**(3): p. 437-445.

103. Naudin, C., J. Frund, and A. Pineau, *Intergranular fracture stress and phosphorus grain boundary segregation of a Mn-Ni-Mo steel.* Scripta Materialia, 1999. **40**(9): p. 1013-1019.

104. ASTM, *ASTM E112-13 - Standard Test Methods for Determining Average Grain Size.*

105. Fralich, R.W., *Experimental investigation of effects of random loading on the fatigue life of notched cantilever-beam specimens of SAE 4130 normalized steel*. 1961: National Aeronautics and Space Administration.

106. Pouranvari, M., *Tensile strength and ductility of ferrite-martensite dual phase steels.* Metalurgija, 2010. **16**(3): p. 187-194.

107. Sawley, K., *Bainitic steels for rails.* TTCI Technology Digest, Transportation Technology Center Inc., Pueblo, CO, USA, 1997.

108. Sorokin, G. and S. Bobrov, *Effect of tempering temperature on the fatigue strength of high-strength tool steel.* Metal Science and Heat Treatment, 1974. **16**(9): p. 755-757.